X-ray micro-tomography and pore network modeling of single-phase fixed-bed reactors.

Faical Larachi, Rachid Hannaoui, Pierre Horgue, Frédéric Augier, Yacine Haroun, Souhail Youssef, Elisabeth Rosenberg, Marc Prat, Michel Quintard

X-ray micro-tomography and pore network modeling of single-phase fixed-bed reactors

F. Larachi [a,*], R. Hannaoui [a], P. Horgue [b], F. Augier [a], Y. Haroun [a], S. Youssef [c], E. Rosenberg [c], M. Prat [b,d], M. Quintard [b,d]

[a] *IFP Energies nouvelles-Lyon, Rond-point de l'échangeur de Solaize, BP 3, 69360 Solaize, France*
[b] *Université de Toulouse, INPT, UPS, Institut de Mécanique des Fluides de Toulouse, allée Camille Soula, 31400 Toulouse, France*
[c] *IFP Energies nouvelles, 1 et 4 avenue Bois-Préau, 92852 Rueil-Malmaison, France*
[d] *CNRS, IMFT, F-31400 Toulouse, France*

GRAPHICAL ABSTRACT

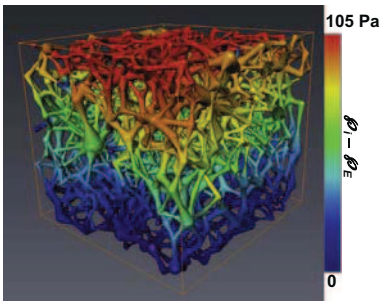

ABSTRACT

A three-dimensional (3D) irregular and unstructured pore network was built using local topological and geometrical properties of an isometric bead pack imaged by means of a high-resolution X-ray computed micro-tomography technique. A pore network model was developed to analyze the 3D laminar/inertial (non-Darcy) flows at the mesoscopic (pore level) and macroscopic (after ensemble-averaging) levels. The non-linear laminar flow signatures were captured at the mesoscale on the basis of analogies with contraction and expansion friction losses. The model provided remarkably good predictions of macroscopic frictional loss gradient in Darcy and non-Darcy regimes with clear-cut demarcation using channel-based Reynolds number statistics. It was also able to differentiate contributions due to pore and channel linear losses, and contraction/expansion quadratic losses. Macroscopic mechanical dispersion was analyzed in terms of retroflow channels, and transverse and longitudinal Péclet numbers. The model qualitatively retrieved the Péclet-Reynolds scaling law expected for heterogeneous networks with predominance of mechanical dispersion. Advocated in watermark is the potential of pore network modeling to build *a posteriori* constitutive relations for the closures of the more conventional macroscopic Euler approaches to capture more realistically single-phase flow phenomena in fixed-bed reactor applications in chemical engineering.

Keywords:
Pore networks
Porous media
Single-phase flow
Non-Darcy flow
Inertial effects
Mechanical dispersion

* Corresponding author. Address: Department of Chemical Engineering, Laval University, Québec, QC G1V 0A6, Canada. Tel.: +1 418 656 3566; fax: +1 418 656 5993.
E-mail address: faical.larachi@gch.ulaval.ca (F. Larachi).

Nomenclature

A_{ij}	channel friction loss per unit length, Pa/m
C_0	laminar constant (Eq. (11)), –
C_{ij}	contraction friction loss, Pa
D_0	laminar constant (Eq. (12)), –
d	particle diameter, m
E_{ij}	expansion friction loss, Pa
Eu_{ij}	channel ij Euler number, –
e	bed porosity, –
g	gravitational acceleration, m/s^2
L_{ij}	center-of-mass distance between two adjacent pores, m
l_{ij}	equivalent channel length, m
m	curvature parameter (Eq. (12)) or number of channels entering a given pore, –
N_c	total number of channels, –
N_p	total number of pores, –
n	curvature parameter (Eq. (11)), –
P_F	network feed pressure, Pa
P_E	network exit pressure, Pa
p'_i	channel static pressure from pore i side, Pa
P_i	pore i static pressure, Pa
$\wp_i$	pore i total head, Pa
Pe_L	longitudinal channel Péclet number, $\langle v_{c\alpha}\rangle/\langle v_{c\alpha}\rangle$, – (same formalism for pore)
Q	cumulative (feed) flow rate, m^3/s
p	number of channels leaving a given pore, –
q_{ij}	channel ij volumetric flux, m^3/s
Re_{bed}	bed (or particle) Reynolds number, $\rho V_s d/(1-e)\mu$, (as in traditional definition of packed-bed friction factor-Re correlations), –
Re_{ij}	channel ij Reynolds number (Eq. (13)), –
r_i	pore i radius, m
r_{cij}	channel ij constriction radius, m
r^e_{cij}	channel ij effective constriction radius, m
r_{minij}	channel ij minimum throat radius, m
U_α	directional unit vector of pore flow (Eq. (27)), –
V_s	superficial velocity, m/s
v_{ij}	channel ij interstitial velocity (Eq. (28)), m/s
$\langle v_{c\alpha}\rangle$	ensemble-average channel ($\alpha = x, y, z$) velocity component, m/s
$\langle v'_{c\alpha}\rangle$	ensemble-average channel ($\alpha = x, y, z$) root-mean-square velocity component, m/s
$\langle v_{p\alpha}\rangle$	ensemble-average pore ($\alpha = x, y, z$) velocity component, m/s
$\langle v'_{p\alpha}\rangle$	ensemble-average pore ($\alpha = x, y, z$) root-mean-square velocity component, m/s
(x_i,y_i,z_i)	pore i center-of-mass coordinates, m

Greek

Γ_{y-}	lower network domain exit boundary
Γ_{y+}	upper network domain entrance boundary
$\gamma_0\cup\gamma_{s0}\cup\gamma_1$	constriction contour
$\gamma_1\cup\gamma_{s1}\cup\gamma_2$	channel contour
$\gamma_2\cup\gamma_{s2}\cup\gamma_3$	expansion contour
Δx	spatial resolution, μm
δ_j	pore j multiplier, –
ε_{ij}	channel ij expansion friction loss factor, –
κ_{ij}	channel ij contraction friction loss factor, –
μ	fluid viscosity, Pa s
ρ	fluid density, kg/m^3
σ	standard-deviation, Table 1
$\underline{\phi}$	volumetric flux objective function vector, m^3/s

Subscript

c	channel
E	exit
F	feed
L	longitudinal
p	pore
T	transverse

Superscript

$'$	relative to channel
$\overline{\ }$	volume average operator (Eq. (23))
(i)→	leaving pore i (Eq. (26))
$\underline{\ }$	vector entity
$=$	matrix entity

Acronym

$\langle\rangle$	ensemble-average operator
3D(2D)	three (two) dimensional
COV	coefficient of variation, Table 1
CSTR	continuous-stirred tank reactor

1. Introduction

Pore network modeling is a remarkably powerful approach which allows linking pore-level transport phenomena to the macroscale flow behavior in porous media [1]. Since its inception with the seminal works by Fatt [2], the literature on pore network modeling has been growing at a phenomenal rate and, hitherto, has imposed itself as a key branch of research on porous media. The breadth of possibilities allowed by pore network modeling extends from procurement of upscaled intrinsic and relative permeabilities [3–5], estimation of hydrodynamic dispersion and mass transfer with or without phase changes [1,6–9], and simulation of quasi-equilibrium and non-equilibrium drainage and imbibition dynamics [10,11], to name just a few topics.

It is the advent of spatially-resolved imaging techniques, such as X-ray computed micro-tomography, that has thrust the capabilities of network modeling to new heights [1]. Nowadays, these techniques enable imaging the 3D pore space of actual porous media with routine spatial resolutions down to a micron [12]. Topologically equivalent backbones are then extracted whereby the irregular poral space is represented in the form of bonds and nodes to which volumes, areas, lengths, and shapes are assigned to mimic the detailed 3D images. Hence, the level of scrutiny, in its default assertion, is meant to depict mesoscale (or pore-level) physics in accordance with which network modeling relies on a collection of simple physical rules, *e.g.*, mass, momentum and energy balances, tinged with the *local* topological and geometrical attributes belonging to each individual pore. Often, pore network modeling refers to instances where the microscale inner-pore-level information is either forgone or compressed in the averaging processes – *e.g.*, in the form of shape factors, flow rates in idealized channel geometry, *etc.* In this regard, pore network modeling bridges the gap between the macroscopic volume-average multi-fluid Euler approaches that necessitate *a priori* knowledge of constitutive relationships [13–16], and the higher-rank CPU-intensive simulation methods, such as lattice Boltzmann [17], smoothed

particle hydrodynamics [18], level set [19], or volume-of-fluid [20–22] methods, which are tractable only at a restricted level of a few pores or for simplified configurations [1]. Pore network modeling is therefore the tool of choice to build *a posteriori* the constitutive relations needed for the description of macroscale flows in porous media, provided the essential features of these latter, borne in topologically equivalent networks, are affordable from highly-resolved 3D visualizations of the pore space.

Specific interest for porous media in chemical engineering firmly rests on a tremendous reliance on fixed-bed reactors which are the work horse of the chemical process industry. Remarkable examples comprise wall-cooled multi-tubular reactors, staged adiabatic beds integrated with heat exchangers/regenerators, simulated moving-bed adsorbers and myriad other applications [22–25]. Despite a vast body of literature which treats fixed bed key issues, such as flow patterns, wall heat transfer coefficients, interphase (fluid to particles) heat and mass transfer [26], studies continue in this area with uninterrupted progress due to their technological importance. Non-Darcy flows are a special class of single-phase flows through porous media which have received extensive coverage in the literature due to their importance particularly in petroleum, in reservoir and in chemical engineering [27–32]. Antagonizing Darcy flows, they take place at high fluid velocities whereby the surge of inertial forces leads to sizeable deviations from (Darcy's law) linear flow rate-pressure gradient dependence. Ergun- or Forchheimer-like relations are the non-Darcy approximations *par excellence* of the macroscale momentum balance for single-phase flow in porous media [31]. Often, their structure is assumed *a priori* and where their linear and quadratic constants are adjusted to match macroscopic frictional pressure drop-flow rate measurements. Such practice remains however clueless as regards the link between fluid flow and the specific micro/mesoscale structures of the porous medium. Hence, conceptual works gradually emerged to capture, more or less with limited success, the microscopic origins of non-Darcy flows based on assumptions as diverse as capillary-orifice [33], representative unit cell [34–36], diverging-converging [37], and disordered porous media [38]. Upscaling techniques were used to understand more fundamentally departures from Darcy's law. If the pore-scale Reynolds number is in the limit of zero, there is a consensus between the different techniques (*e.g.*, homogenization theory, volume averaging) on the emergence of a full anisotropic Darcy's law with so-called closure problems allowing access to the permeability tensor from the micro-structure [39,40]. An increase in the Reynolds number leads to the following sequence. First, small departure from Darcy's law, hereafter denoted as the weak inertia regime, starts with a cubic correction contrary to the quadratic modification in the classical form of Forchheimer's law [30,41–43]. When the Reynolds number increases further strong inertia effects start to produce some effects. Forms of the macro-scale equations were obtained for strong inertia effects long before truly-established pore-scale turbulence. The macroscale equation obtained by Whitaker [44] has a non-linear additional inertia term under the form of a generalized Forchheimer term: a fully anisotropic and non-linear tensor, for which a closure problem exists, that is multiplied by the filtration velocity. The correction is not necessarily quadratic as illustrated in Lasseux et al. [43]. Indeed, in the case of simple representative unit cells or so-called non-disordered media, the weak inertia cubic correction may hold for a large range of Reynolds number and the classical quadratic form is not a very good approximation and anisotropic effects due to the velocity orientation are strong. In this same work, things go better in favor of a quadratic correction when using highly disordered unit cells or randomly distributed arrays as thoroughly discussed in the recent work by Yazdchi and Luding [45]. When one increases the Reynolds number, true turbulence begins to appear at the pore-scale, thus allowing to treat the upscaling problem in two sequential upscaling steps: the first one to get a pore-scale turbulent model (*e.g.*, RANS), the second step a volume averaging of the turbulent equations [14,46,47]. This stage is beyond the scope of this work; however, it is interesting to notice that, if one takes Navier–Stokes equations with a spatially distributed *turbulent* viscosity, then the volume averaged equation has the form of the generalized Forchheimer equation proposed in Whitaker [44]. Application of the theory to structured packings suggests a non-quadratic correction for a wide range of Reynolds numbers consistent with the findings of Lasseux et al. [43] for non-disordered media.

Only a few studies have hitherto focused on descriptions of non-Darcy flows with recourse to pore network modeling. Thauvin and Mohanty [48] were the first to implement a computer-generated regular hexa-coordinated cubic lattice to test the effect of converging–diverging pore segments, pore connectedness, and distribution of pore sizes. Topology of such a network was quite afar from realistic unstructured and irregular networks [1,49]. Using simplified contraction/expansion/bend friction loss factors applicable for fully-turbulent flows, these authors reconstructed pressure gradient with quadratic velocity dependence in qualitative agreement with Ergun/Forchheimer expressions. In further efforts, Wang et al. [50] altered the above regular lattice network *via* size-induced, connectivity-induced and spatial correlation-induced anisotropy to approach the behavior of actual unstructured/irregular networks. 2D networks of cylindrical pipes with randomly generated sizes were also computer-generated by Lao et al. [51] to represent a porous medium. Quadratic velocity effects formally similar to those used by Thauvin and Mohanty [48] and Wang et al. [50] were evidenced at the pore splitting as mostly responsible for non-Darcy flow behavior. It is noteworthy that these approaches implemented asymptotic turbulent limits of the contraction and expansion loss coefficients given by Bird et al. [52] which are not valid for channel $Re < 10^4$. Along the same vein of 2D statistical networks, Martins et al. [53] recently proposed an approach based on the same incompatible assumption of turbulent correlations in laminar flow regime. Therefore, recovery in the macroscopic forms of the local quadratic terms is merely pleonastic and not consistent with non-turbulent non-Darcy flow deviations. As a matter of fact, non-Darcy flows occur at bed Reynolds numbers as low as *ca.* 10 [54] while inception of turbulence in porous media – consisting of mm-sized bead packs – requires bed Reynolds numbers >600 [55]. Therefore, it is unlikely that turbulent flows would prevail in the pore-network channels under typical porous media operation. Balhoff and Wheeler [56], on the principle, cleverly addressed this limitation by implementing a finite element method and then fitting empirical functions between poral pressure drop and flow rate. However, the laminar Navier–Stokes equations were solved by approximating pore throats as *symmetrical* sinusoidal ducts, that is by imposing as a geometrical simplification equal distances (and channel radii) up and downstream of the pinch. This simplification may not accurately capture the actual intrinsic lack of symmetry in local throat geometry. Hence, more representative closures of non-turbulent non-linear dissipations at pore-throat-pore junctions must be built and tested in pore network simulations.

Our study's main objective will be to investigate qualitatively and quantitatively non-Darcy single-phase flow for real unstructured and irregular three-dimensional networks. To reach our goal, the following methodology will be pursued throughout this work: (i) implement micro-tomography measurement of a randomly packed non-consolidated porous medium consisting of isometric mm-size spheres; (ii) extract a pore network with its thorough topological and geometrical characterization; (iii) establish rigorous mesoscopic mechanical energy balances and formulate representative constitutive laws for pore-throat-pore flows; (iv) define

and compute the upscaled variables for an evaluation of the porous medium macroscopic behavior; (v) assess the contribution of quadratic dissipation and its distinction from acceleration/deceleration effects at pores entrance and exit; (vi) quantify the contributive components to the macroscopic frictional head loss gradient; and finally (vii) analyze the influence of network heterogeneity on mechanical dispersion.

2. Experimental

2.1. Imaging & reconstruction

A sample porous medium was prepared by packing monodisperse 4-mm spherical glass beads in a small container with an overall bed porosity of 36 %. The actual three-dimensional (3D) pore structure of the thus realized porous specimen, with air occupying its interstices, was imaged using X-ray computed μ-tomography. The IFPEN X-ray Phoenix Nanotom high-resolution facility was used to generate as many two-dimensional (2D) projections as necessary by rotating the X-ray source around the specimen being imaged. Angular increments as narrow as 0.2° are easily achievable yielding up to 1800 projections for a 360° sweep to enable high-resolution numerical reconstruction of the volumetric data. The 2D projections consisting of 2304×2304 pixels were detected on a 110×110 mm^2 Hamamatsu flat detector with a 50 μm step excited under tube voltage bias and current of *ca.* 90 kV and 170 μA, respectively. Beam hardening effects were corrected using metal Cu filter and *post-facto* corrections during reconstruction [57]. After completing data acquisition, the projections were stacked and post-processed using a cone-beam Feldkamp algorithm [58] to reconstruct high-resolution gray-level density maps of the 3D domain. The size of the reconstructed domain was $3.06_x \times 2.76_y \times 3.04_z$ cm^3 with a unitary resolution voxel $\Delta x \times \Delta y \times \Delta z = 40^3$ μm^3 and a 3D image composed of $765 \times 690 \times 760$ voxels.

2.2. Extraction of pore network

A pore network extraction methodology was subsequently applied to convert the 3D density maps into resolved pore space [57]. It enabled partition of poral space into pore bodies, pore throats, channel lengths, and pore–pore connectivities. Conversion of 3D maps went through the following 4-step procedure: segmentation, skeletonization, pore space partitioning (and throat detection) and parameters extraction.

Segmentation was implemented to resolve the inter-granular void voxels from their solid phase (material) counterparts. For image segmentation, trial-and-error thresholding was applied on the gray-level frequency distributions to resolve local porosity [57]. A binarization process of grey levels was adopted ascribing unit porosity to void space and nil porosity to solid phase. Subsequent to thresholding, filtering (removal of islands) and morphological operations (smoothing, shrinking and growing) were implemented. A binary 3D image of each phase (solid and void) was generated giving access to local void volumetric fraction and spatial distribution. Fig. 1 exposes the complex topology of the reconstructed void space imprinted by randomly filling the domain with 4-mm glass beads. This void already highlights reminiscences of pores and throats to be resolved in the later steps by extracting *ad hoc* pore network topological and geometrical parameters.

As a subsequent post-processing step, skeletonization of the segmented domain was obtained by generating a skeleton of the porous medium from interconnecting the void space voxels using an extraction algorithm. Originally developed for extracting brain microcirculation networks [59,60], this algorithm implements distance ordered homotopic thinning and was extended to network

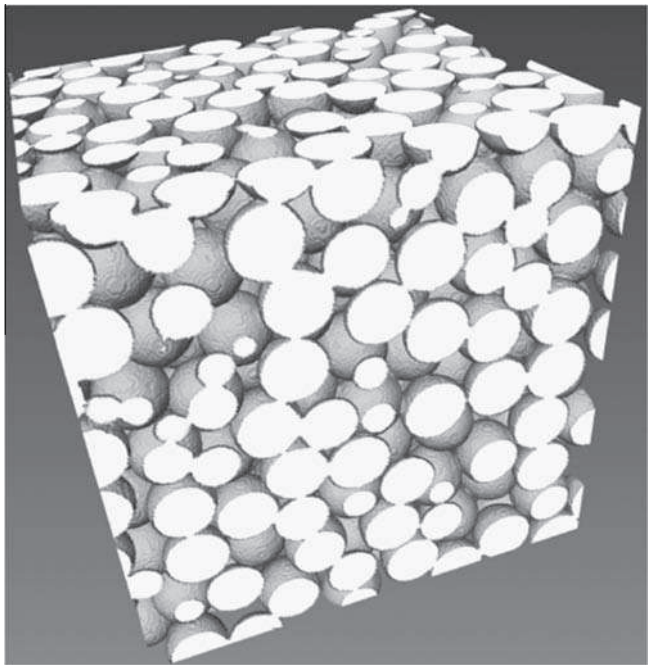

Fig. 1. Three-dimensional reconstruction of the porous parallelepipedic specimen (consisting of 4-mm glass beads) sampled using 2D microtomography scans.

extraction of pore space in rock analyses [57,58,61]. The algorithm's output, in this latter outgrowth, enabled building a distance map to assign to each voxel of the skeleton a minimum distance to the void space boundary.

A pore space partitioning algorithm was then used to map the void space from the skeleton network into nodal throat-sharing pores inter-connected *via* channels [57]. The algorithm main tasks consisted in (a) identifying the lines describing channels, detecting and locating throat points, (b) partitioning and labeling the skeleton into groups of lines pertaining to the same pore bodies, and (c) reconstructing and separating the labeled pore bodies using a voxel growth constrained algorithm.

To allow flow computations, the final step of the pore network extraction methodology enabled assigning topology and geometry metrics to the pore space resolved in terms of pore volumes, throat surfaces and lengths. This was made possible upon evaluation of the following quantitative parameters from the 3D pore space images:

(a) Pore-*i* body: It is objectified by its volume evaluated from a voxel-growth constrained algorithm and its center of mass (x_i, y_i, z_i), CoM. In terms of shape, all pore bodies in the network were isomorphic and attributed a common spherical shape. Hence each pore radius, r_i, is that of the equivalent isovolume sphere.

(b) Connectivity of pore bodies: It is evaluated in terms of a coordination number, *i.e.*, number of adjacent pores interconnected to pore-*i* body *via* its peripheral throats.

(c) Pore throat radii: Two properties are evaluated for intersecting pores *i* and *j* along channel *ij* to characterize, respectively, the minimum radius, r_{minij}, of each throat and a constriction radius, r_{cij}, based on the ratio of throat cross-section area to its perimeter. The minimum radius corresponds to the largest collapsible sphere to be inscribed in the throat cross section whereas circularly shaped throats are assumed in calculating r_{cij}. Moreover, throats, in a first approximation, are viewed as 0-volume constrictions despite they are endowed with channel lengths as a

necessary condition to give rise to *regular* inter-pore pressure drop terms. Thus all the volume content will be assigned to poral bodies.

(d) Hydrodynamic channel length: It is that of an equivalent cylindrical channel extending back and forth around throat *ij*. Actual channels, as unveiled from Fig. 1, are not cylindrical but rather of a biconical (converging–diverging) shape. Thus, to capture in a more representative manner the flow hydraulics and corresponding regular pressure drop in the connecting channel, actual channels can be approximated by a series of "telescopic" elementary (voxel-thick) sheets of variable radii stacked perpendicularly to r_{minij} and extending around the throat locus, r_{minij} [57]. Assumption of Poiseuille dependence between elementary sheet conductance, sheet radius r_k and thickness l_k, enables determining the equivalent cylindrical channel length as follows:

$$l_{ij} = \sum_k l_k \left(\frac{r_{\min,ij}}{r_k} \right)^4 \quad (1)$$

Fig. 2a and b are 3D illustrations of the pore network extracted using the above methodology. The specificities of the bead pack are clearly represented in terms of pore connectivities, throat lengths and radii, and pore bodies as depicted by their isovolume spherical proxies in Fig. 2b.

2.3. Network topology and geometry

Fig. 3a–f depict the frequency and cumulative distributions of, respectively, pore connectivity, angular tilt of channel (from inclination of CoM line of connected pore pairs), pore radius, constriction radius, r_{cij}, minimum constriction radius, and equivalent cylindrical channel length extracted from the binary images. The main topology and geometry descriptors of the pore network are summarized in Table 1 in terms of average, standard deviation and coefficient of variation (*COV*) figures. The total void volume retrieved from Fig. 3a cumulative volume frequency distribution of Fig. 2a pore network domain amounted to a computed overall bed porosity of 37.3%.

The pore space was composed of $N_p = 1213$ pores connected through throats *via* $N_c = 2475$ channels. The average values of pore radius, constriction radius, minimum constriction radius, equivalent channel length and connectivity amounted, respectively, to 1.06 mm, 0.46 mm, 0.13 mm, 0.93 mm and 4.1. The r_{cij}/r_i ratios spanned the range $[8.78 \times 10^{-3}–1.0]$ with an average ratio of 0.41. It should be noted that for a few instances (35 out of 2475) a small range of the r_{cij}/r_i distribution exceeded the upper physical limit of 1. This was attributed to artifacts either in image reconstruction or in pore network extraction. Those instances were kept in the ensemble but their r_{cij}/r_i ratios were reduced to one. Similarly, the l_{ij}/r_{cij} ratios swept the range [0.17–94.4] with an average length-to-radius ratio of 2.68. As regards the channel inclinations, they were computed on the basis of the connecting pore body centroids. Channel tilts displayed a bell-shape curve where close-to-vertical channels outnumber the distribution as seen in Fig. 3b.

The pore network model requires minimally doubly-coordinated pores for fluid flow simulations. In Fig. 3a, the distributions of coordination are expressed in terms of number and void volume fractions. Very few pores, *ca.* 2.1% (number percent), were highly coordinated from 12 to 20 and contributed *ca.* 5.9% of the bed porosity. At the opposite side of the spectrum, 3.0% of the pores were singly-coordinated. Accounting for a tiny 0.14% bed porosity, they were disseminated both in the domain core and alongside its boundaries. However, those in the core were considered as orphan pores and were ignored in the flow simulations. Doubly-coordinated pores sharing channels with orphan pores were likewise disabled. All flow-forbidding pores accounted for only 0.16% of the bed overall porosity. However, a large proportion of pores, *i.e.*, 71.7%, displayed 2–4 coordinations contributing 13% of the bed porosity (Fig. 3a). Topologically, the obtained pore network is a 3D irregular unstructured network [49]. Indeed, the network features an irregular coordination pattern (Fig. 3a) with multiple orientations of throats deviating from the three principal directions of a regular lattice; thus the network unstructured character. Also, due to large disparities in pore sizes, the pore centers of mass cannot be located on equally-spaced lattice nodes; thus the network irregular character.

Most of the *peripheral* pore bodies located at the domain entrance (Γ_{y+}) and exit (Γ_{y-}) boundaries are interconnected to other peripheral pore bodies, in addition to being coordinated to some inner (core) pore bodies (Fig. 4a and b). Such interconnectedness enables cross-flows to occur among pores located on the same boundary. The vast majority of boundary pore bodies (*ca.* 98–99%) were coordinated to nearby boundary pore bodies by

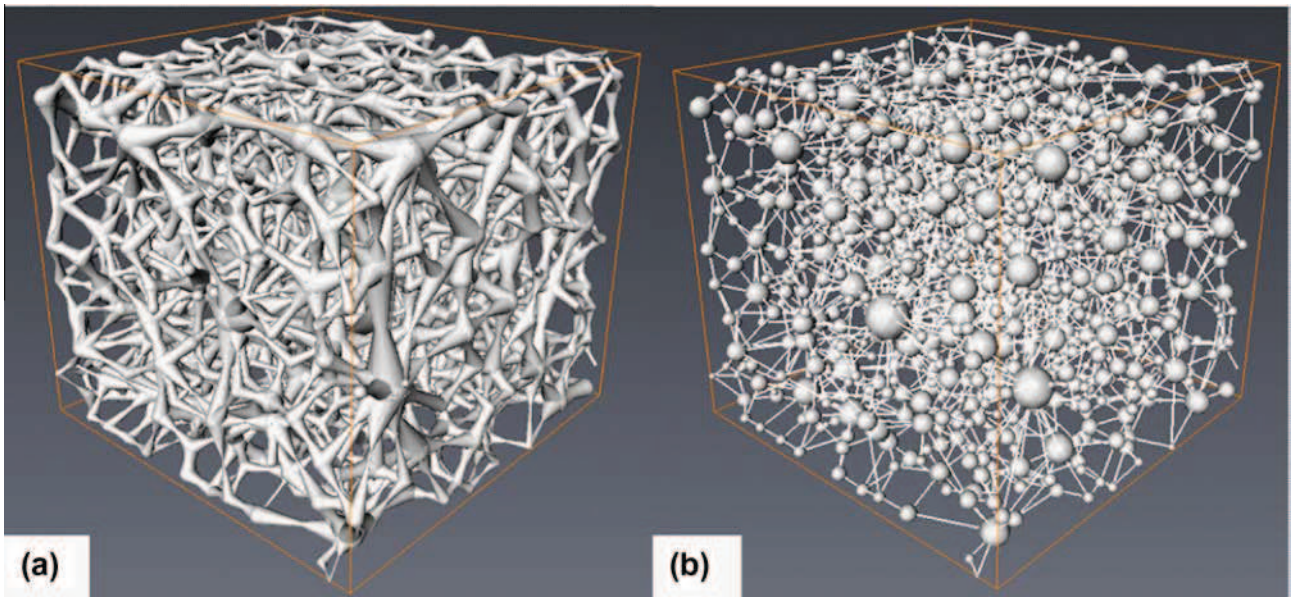

Fig. 2. 3D representation of the pore network in terms of pore connectivities, throat radii and lengths (a) and pore volumes of equivalent spheres (b).

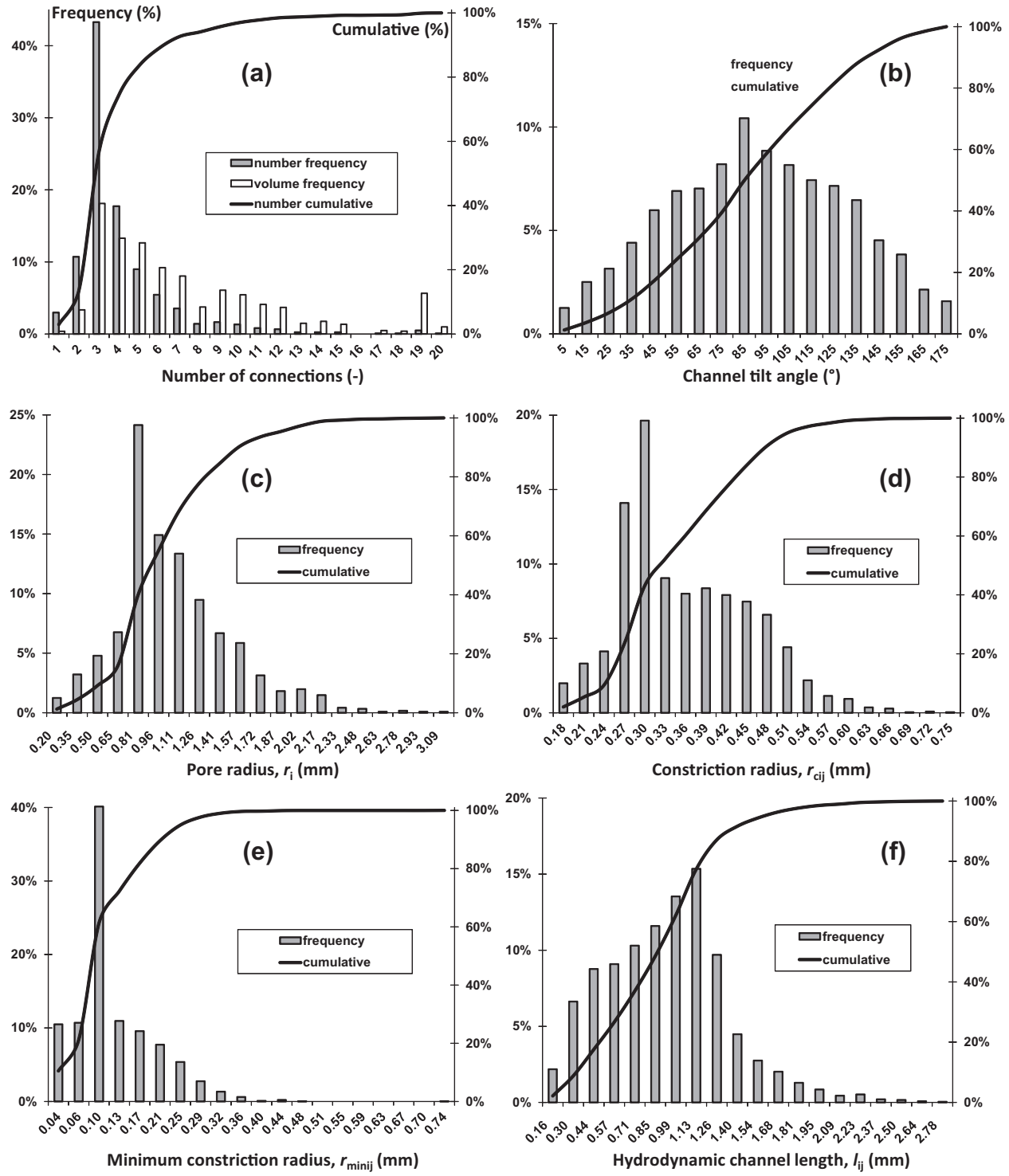

Fig. 3. Frequency and (ascending) cumulative distributions of pore connectivity (a), angular inclination of channels (b), pore radius (c), constriction radius (d), minimum constriction radius (e) and equivalent (or hydrodynamic) cylindrical channel length (f).

involving up to 7 connections. This peculiarity must not be ignored in formulating the pore network boundary conditions.

3. Theory

3.1. Mesoscopic mechanical energy and mass balances in pore-throat-pore elements

Relations need to be built for expressing the dependence between the fluid volumetric fluxes across the pore network constrictions and the associated head losses stemming from the transit of fluid between the throat-subtending pores. These relations will be elaborated on the basis of zonal mesoscopic mechanical energy balances for incompressible flows performed on each pore (i)-throat (ij)-pore (j) element of the pore network as depicted in Fig. 5a. The interconnected pores, represented by their isovolume spherical proxies, communicate through a circular and volumeless throat, the equivalent length of which is given by the hydrodynamic channel length, l_{ij}, introduced earlier. A flow is assumed to prevail in this geometry where for a given fluid volumetric flux,

Table 1
Summary of network topology and geometry descriptors.

	< >	σ	COV (–)
Pore radius (mm)	1.06	0.43	0.40
Pore volume (mm^3)	7.80	11.2	1.43
Inter-pore CoM distance (mm)	3.09	1.37	0.44
r_i/r_j (–) up-to-downstream	1.48	1.07	0.72
Coordination number (–)	4.1	2.5	0.60
Throat radius (mm)	0.46	0.22	0.48
Equivalent channel length (mm)	0.93	0.41	0.45
r_{cij}/r_i (–) upstream pore	0.37	0.20	0.55
r_{cij}/r_j (–) downstream pore	0.45	0.23	0.51
Throat aspect ratio, l_{ij}/r_{cij} (–)	2.68	3.19	1.19

$\langle\ \rangle$ = average; σ = standard deviation; COV = coefficient of variation = $\sigma/\langle\ \rangle$.

q_{ij}, a pressure profile develops as a result of the dissipations undergone in the contraction, the throat and the expansion, Fig. 5a and b. Depending on the network microstructure which regulates the resistance to flow in the neighborhood of the pore-throat-pore element, both flow modalities, namely, descending and ascending, are plausible at the pore-throat-pore level. Regardless of the local direction of flow, the total head losses are computed as the total head from upstream pore i minus that for downstream pore j. Such a convention implies that head losses take positive values whichever flow modality. To handle the two possible flow modalities, the sign of y_i–y_j determines the relative position of upstream pore i vis-à-vis downstream pore j. Moreover, fluid state in the pore is isobaric except in the vicinity of the contraction and expansion at the throat junction whereby singular pressure drops may arise at sufficiently high Reynolds numbers (Fig. 5b).

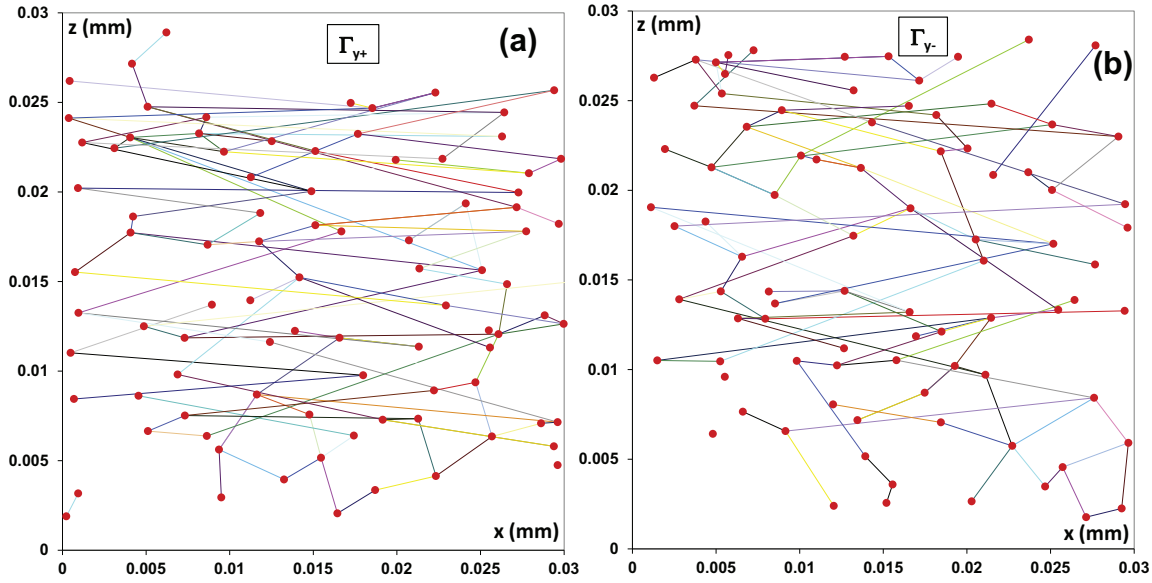

Fig. 4. (x, z) Coordinates of centers of mass of boundary pore bodies at boundaries Γ_{y+} (a) and Γ_{y-} (b). Colored lines illustrate channel interconnectedness among peripheral pore bodies. (For interpretation of the references to color in this figure legend, the reader is referred to the web version of this article.)

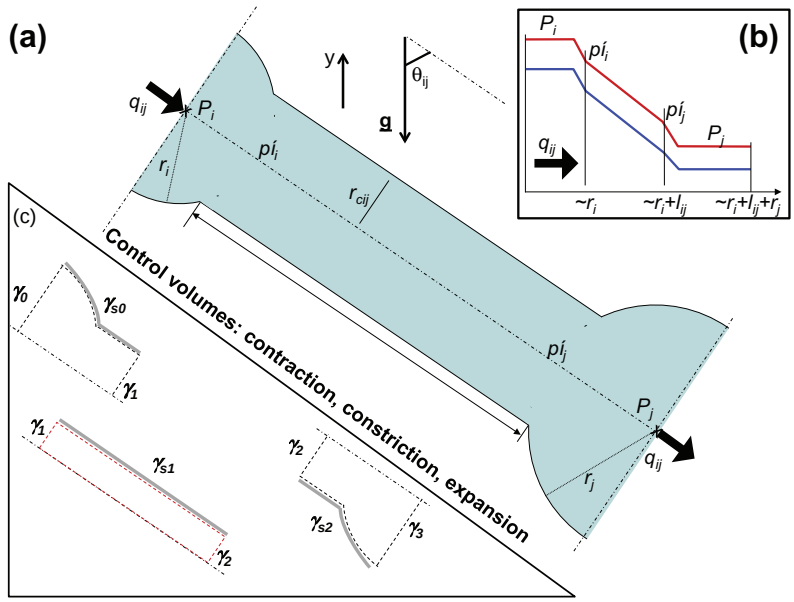

Fig. 5. Pore (i)-throat (ij)-pore (j) element (a), typical pressure profiles due to contraction, constriction and expansion dissipations (b), control volumes for performing mesoscopic mechanical energy balances.

In the contraction zone (Fig. 5c), the fluid control volume is delineated by the contours $\gamma_0 \cup \gamma_{s0} \cup \gamma_1$ to include the friction losses due to contraction as the fluid is about to engulf into the throat. Constriction contour is likewise deployed to encompass the $\gamma_1 \cup \gamma_{s1} \cup \gamma_2$ region to grasp the linear laminar dissipation of Poiseuille flow in a cylindrical tube. Finally, the expansion zone consists of $\gamma_2 \cup \gamma_{s2} \cup \gamma_3$ contour to circumscribe the throat discharging flow. This zone causing friction losses due to expansion is treated similarly to the contraction.

Linear laminar dissipation terms are accounted for in throats and pores to reflect their contribution to the well-known Darcy term in the overall bed pressure gradient. Likewise, quadratic effects are reminiscent of singular pressure drop stemming from flow contraction from upstream pore to throat *ij* and then from flow expansion from throat *ij* to downstream pore (Fig. 5). In what follows, steady-state mesoscopic mechanical energy balance equations will be written for each zone of the pore-throat-pore elements, while in a subsequent step, the needed closure relations will be established.

Fluid mechanical energy balance in $\gamma_0 \cup \gamma_{s0} \cup \gamma_1$ contraction:

$$\frac{\chi}{2\pi^2}\rho q_{ij}^3\left(\frac{1}{r_i^4}-\frac{1}{r_{cij}^4}\right)+\rho g q_{ij}(y_i-y_i')+q_{ij}(P_i-p_i')-C_{ij}q_{ij}=0 \tag{2}$$

The constant χ in Eq. (2) results from expressing the bracketed (average) cubic velocity by the corresponding cube of bracketed (average) velocity. It varies between 2 (laminar parabolic profile) and 1 (nearly flat turbulent velocity profile) and is taken to be the same for the pore and the throat. Also, C_{ij} stands for the contraction frictional losses at entering pore *i*.

Fluid mechanical energy balance in $\gamma_1 \cup \gamma_{s1} \cup \gamma_2$ throat:

$$q_{ij}\left(p_i'-p_j'\right)+\rho g q_{ij}\left(y_i'-y_j'\right)\underbrace{-2\pi l_{ij}\mu\int_0^{r_{cij}}\left(\frac{\mathrm{d}v_{ij}}{\mathrm{d}r}\right)^2 r\mathrm{d}r}_{-A_{ij}l_{ij}q_{ij}}=0 \tag{3}$$

In Eq. (3), A_{ij} is the frictional loss contributed by the throat fluid flow, the expression of which for a circular throat is straightforward to derive:

$$A_{ij}=\frac{8}{\pi}\frac{\mu q_{ij}}{r_{cij}^4} \tag{4}$$

Fluid mechanical energy balance in $\gamma_2 \cup \gamma_{s2} \cup \gamma_3$ expansion:

$$\frac{\chi}{2\pi^2}\rho q_{ij}^3\left(\frac{1}{r_{cij}^4}-\frac{1}{r_j^4}\right)+\rho g q_{ij}(y_j'-y_j)+q_{ij}(p_j'-P_j)-E_{ij}q_{ij}=0 \tag{5}$$

In Eq. (5), E_{ij} is the expansion frictional loss at exiting pore *j*.

In the total head are embedded the velocity head (or kinetic energy), elevation head (gravitational force) and static pressure. The fluid total head for any pore *i* is defined as:

$$\wp_i=\frac{\chi}{2\pi^2}\frac{\rho q_{ij}^2}{r_i^4}+\rho g y_i+P_i \tag{6}$$

Combining Eqs. (2)–(5) and after dividing by q_{ij} yields an expression for the total head loss across the pore-throat-pore assemblage:

$$\wp_i-\wp_j=A_{ij}l_{ij}+C_{ij}+E_{ij} \tag{7}$$

Pore-level mesoscopic mass balance equations are also needed for evaluating the poral pressure field. Casting Krichhoff's current law for the fluid around pore *i*, one obtains:

$$\sum_k q_{ik}=0 \tag{8}$$

where in Eq. (8), the (positive) fluxes leading into pore *i* from an upstream pore *k* are discriminated from those (negative) leading out of pore *i* into a downstream pore *k*. Such directional behavior of fluxes also accounts for the fact that not all throats in the network will discharge in a descending manner, despite prevalence of a macroscopic downflow. Hence, whether the least penalizing flow across throat is upwards or downwards, the model handles local descending and ascending instances alike.

3.2. Constitutive equations for contraction and expansion friction loss factors

Contraction frictional losses, C_{ij}, are expressed for fluid displacement from upstream pore *i* to throat *ij* by introducing friction loss factors κ_{ij} to account for γ_0/γ_1 areal reductions, Fig. 5c. Similarly, expansion frictional losses, E_{ij}, are cast in terms of fluid motion from throat *ij* to downstream pore *j* *via* friction loss factors ε_{ij} for consideration of γ_2/γ_3 areal increases. These expressions are derived by analogy with traditional single-phase flow formulations for obstacles contributing to friction losses. Friction losses are written as a proportionality function of velocity head in the throat and a friction loss factor (Table 2). Considering the range of velocities in porous media, friction loss factors must be constructed to encompass linear laminar, laminar inertial and eventually turbulent flows depending on pore-throat areal ratios and throat Reynolds numbers. Hence, the contraction and expansion friction losses have been constructed to preserve asymptotic consistency both at creeping and turbulent flow limits using friction loss factor databases tabulated in Idel'chik [62] for contraction and expansion flows. Passages from upstream pore to throat and from throat to discharging pore are treated as sharp areal transitions. Table 2 summarizes the ensemble of relations derived for single-phase flow in the pore network.

3.3. Network boundary conditions

Fig. 6 sketches the boundary condition approach adopted to handle the top feed and bottom exit fluid streams traversing the pore network. The exit pressure P_E is assumed to be known *a priori*, whereas the cumulative fluid flow rate, Q, is imposed at the entrance in a downflow setting along the y direction. As discussed above, channels of varying constriction radii and lengths link boundary pore bodies to each other (dotted lines, Fig. 6) enabling pressure-driven flows to take place among them. Peripheral pores will thus adjust individually their pore pressures along Γ_{y+} boundary depending, among other variables, on the fraction of flow rates received from the feed manifold (viewed as an entrance mega-pore) positioned atop at elevation y_F and wherefrom the total payload is delivered at a constant feed pressure, P_F. Likewise, the pore bodies occupying Γ_{y-} boundary deliver their fractional flow rates to an exit receptacle (viewed as an exit mega-pore) located at

Table 2
Expressions of contraction/expansion friction loss factors.

Contraction friction loss from pore *i* to throat *ij* $C_{ij}=\frac{\rho}{2\pi^2}\frac{q_{ij}^2}{r_{cij}^4}\kappa_{ij}$	(9)
Expansion friction loss from throat *ij* to pore *j*: $E_{ij}=\frac{\rho}{2\pi^2}\frac{q_{ij}^2}{r_{cij}^4}\varepsilon_{ij}$	(10)
Contraction friction loss factor from pore *i* to throat *ij*: $\kappa_{ij}^n=\left(\frac{C_0}{\mathrm{Re}_{ij}}\right)^n+\frac{1}{2^n}\left(1-\frac{r_{cij}^2}{r_i^2}\right)^n$	(11)
Expansion friction loss factor from throat *ij* to pore *j*: $\varepsilon_{ij}^m=\left(\frac{D_0}{\mathrm{Re}_{ij}}\right)^m+\left(1-\frac{r_{cij}^2}{r_j^2}\right)^{2m}$	(12)
Throat-based Reynolds number: $\mathrm{Re}_{ij}=\frac{2}{\pi}\frac{\rho q_{ij}}{\mu r_{cij}}$	(13)

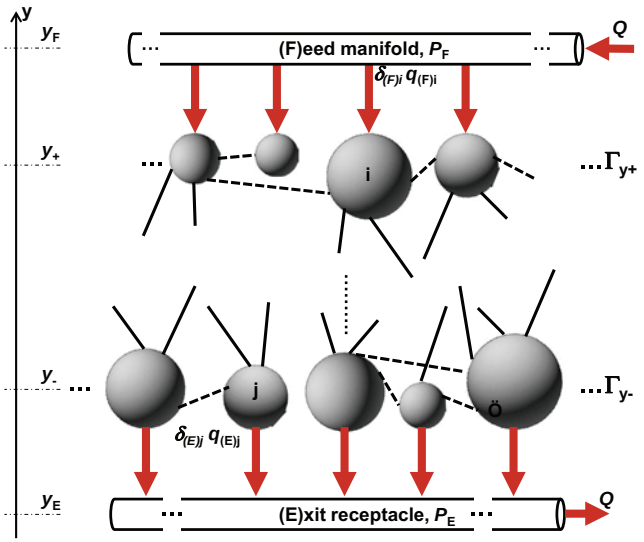

Fig. 6. Channels connecting feed manifold & exit receptacle (red arrow), Γ_{y+} & Γ_{y-} boundary pore bodies (dotted line), and core pore body/ies. (For interpretation of the references to color in this figure legend, the reader is referred to the web version of this article.)

elevation y_E kept at a known exit pressure P_E (Fig. 6). The remaining 4 faces of the pore network are impervious to fluid *lateral* leakages. Kirchhoff's law is then applied such that the algebraic sum of fluxes meeting at each pore of the network is zero. Feed/exit maldistribution due to some dysfunctional inlet or outlet pores, *e.g.*, pore plugging, can optionally be simulated by defining boundary condition pore multipliers, δ_j, as shown in Eqs. (14)–(19) below.

Flux conservation around feed manifold and exit receptacle:

$$Q - \sum_{j\in\Gamma_{y+}} \delta_{j(F)} q_{(F)j} = 0; \quad \delta_{j(F)} = \begin{cases} 0 & \text{pore inlet blocked} \\ 1 & \text{otherwise} \end{cases} \tag{14}$$

$$Q - \sum_{j\in\Gamma_{y-}} \delta_{j(E)} q_{(E)j} = 0; \quad \delta_{j(E)} = \begin{cases} 0 & \text{pore exit blocked} \\ 1 & \text{otherwise} \end{cases} \tag{15}$$

where $q_{(F)j}$ and $q_{E(j)}$ are the flow rates in the virtual channels, wherein only laminar dissipation occurs, which connect boundary pores j (belonging to boundary Γ_{y+} or Γ_{y-}) to feed or exit mega-pore:

$$q_{(F)j} = \frac{\pi r^4_{\Gamma_{y+}j}(P_F - P_{\Gamma_{y+}j} + \rho g(y_F - y_{\Gamma_{y+}j}))}{8\mu(y_F - y_{\Gamma_{y+}j})} \tag{16}$$

$$q_{(E)j} = \frac{\pi r^4_{\Gamma_{y-}j}(P_{\Gamma_{y-}j} - P_E + \rho g(y_{\Gamma_{y-}j} - y_E))}{8\mu(y_{\Gamma_{y-}j} - y_E)} \tag{17}$$

Flux conservation around pore j belonging to boundary Γ_{y+} (respectively, Γ_{y-}) interconnected to m in-flow and p out-flow pores:

$$\delta_{j(F)} q_{(F)j} + \sum_{k=1}^{m} q_{kj} - \sum_{l=1}^{p} q_{jl} = 0 \tag{18}$$

$$-\delta_{j(E)} q_{(E)j} + \sum_{k=1}^{m} q_{kj} - \sum_{l=1}^{p} q_{jl} = 0 \tag{19}$$

3.4. Averaging procedure

The pore network simulation outputs consist of *primary* local-scale variables such as (pore scale) static pressures or total heads, and (channel scale) fluxes or velocity vectors. *Secondary* local variables can also be defined; for instance, pore scale fluxes or velocity vectors. Macroscopic analogs can be derived from averaging these local variables over boxes extendable to comprise the entire network domain. Also, an overall head loss, *i.e.*, *frictional* pressure gradient across the whole network along y direction, is obtained as the difference between the intrinsic macroscopic averages, that is the volume-average total heads at Γ_{y+} and Γ_{y-} boundaries [11,15] divided by their average separating distance (Eq. (23), Table 3). The gravity term hidden in the pressure head is written to account for the whole fluid mass in the pore and not only that in the channel; hence recourse to a pore CoM difference, y_i–y_j (Eq. (6)). It will be verified later that the contribution of velocity head to the total head is vanishingly small and that most of the total head is due to static pressure and elevation head.

The ensemble-average channel 3D ($\alpha = x, y, z$) velocity components ($\langle v_{c\alpha}\rangle$) and their corresponding root-mean square velocity ($\langle v'_{c\alpha}\rangle$) components are evaluated over the entire network domain according to standard definitions (Eqs. (26) and (27), Table 3). In these equations, the channel velocity components along pore-throat-pore direction ij are related to the channel flow rate as follows:

$$v_{ij} = \sqrt{v^2_{x,ij} + v^2_{y,ij} + v^2_{z,ij}} = \frac{q_{ij}}{\pi r^2_{c,ij}} \tag{23}$$

A similar treatment applied to pore entities yields ensemble-average velocity, $\langle v_{p\alpha}\rangle$, components and their corresponding root-mean square velocity, $\langle v'_{p\alpha}\rangle$, components (Eqs. (29) and (30), Table 3). Note that pore velocity is not a direct output of the pore network model but requires specific hypotheses for its formulation. The first rests on the fact that the fluid velocity field is a continuous function nearby the pore CoM. The second, pore velocity is equally estimable either from m upstream channel velocity components entering into the pore or from p downstream channels leaving the pore. Third, a velocity direction is needed within the pore. Hence, the 3D ($\alpha = x, y, z$) poral velocity components are defined using the out-flow convention as follows where the symbol "(i)→" stands for the p channels leaving pore i:

$$v_{p\alpha,i} = \frac{\sum_{j=1}^{p} q_{ij}^{(i)\mapsto}}{\pi r_i^2} U_{\alpha,i} \tag{26}$$

In this equation, $U_{\alpha,i}$ is the α-component of a unit vector dictating the flow direction within the pore. It is calculated as a throat-flux-weighted quantity averaged over the p discharging channels connected to pore i, see Fig. 7. For x-direction for instance, one obtains:

Table 3
Expressions of the macroscopic entities derived from pore-level predicted properties.

Macroscopic head loss gradient $\frac{\bar{\varphi}_{\Gamma_{y+}} - \bar{\varphi}_{\Gamma_{y-}}}{y_{\Gamma_{y+}} - y_{\Gamma_{y-}}} = \frac{\frac{\sum_{j\in\Gamma_{y+}} r^3_{pj} v_j}{\sum_{j\in\Gamma_{y+}} r^3_{pj}} - \frac{\sum_{k\in\Gamma_{y-}} r^3_{pk} v_k}{\sum_{k\in\Gamma_{y-}} r^3_{pk}}}{\frac{\sum_{j\in\Gamma_{y+}} r^3_{pj} y_j}{\sum_{j\in\Gamma_{y+}} r^3_{pj}} - \frac{\sum_{k\in\Gamma_{y-}} r^3_{pk} y_k}{\sum_{k\in\Gamma_{y-}} r^3_{pk}}}$	(20)
Ensemble-average channel 3D ($\alpha = x, y, z$) velocity components: $\langle v_{c\alpha}\rangle = \frac{1}{N_c}\sum_{i,j} v_{\alpha,ij}$	(21)
Ensemble-average channel 3D ($\alpha = x, y, z$) root-mean square velocity components: $\langle v'_{c\alpha}\rangle = \sqrt{\frac{1}{N_c}\sum_{i,j}(v_{\alpha,ij} - \langle v_{c\alpha}\rangle)^2}$	(22)
Ensemble-average pore 3D ($\alpha = x, y, z$) velocity components: $\langle v_{p\alpha}\rangle = \frac{1}{N_p}\sum_{i}^{N_p} v_{\alpha,i}$	(24)
Ensemble-average pore 3D ($\alpha = x, y, z$) root-mean square velocity components: $\langle v'_{p\alpha}\rangle = \sqrt{\frac{1}{N_p}\sum_{i}^{N_p}(v_{\alpha,i} - \langle v_{p\alpha}\rangle)^2}$	(25)

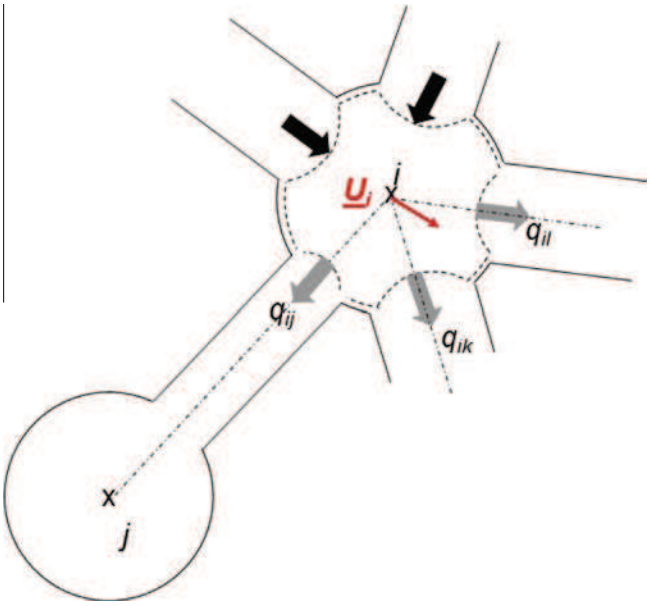

Fig. 7. Directional assignment of pore velocity on the basis of directions of out-flow channels weighted by their corresponding volumetric fluxes.

$$U_{x,i} = \frac{\sum_{j=1}^{p} \frac{\left[q_{ij}^{(i)\mapsto}\right]^2}{L_{ij}\sum_{j=1}^{p}\left[q_{ij}^{(i)\mapsto}\right]^2}(x_j - x_i)}{\|U_i\|} \tag{27}$$

where the CoM distance, L_{ij}, and the pore directional vector, $\underline{U}_i$, are defined as:

$$L_{ij} = \sqrt{(x_j - x_i)^2 + (y_j - y_i)^2 + (z_j - z_i)^2} \tag{28}$$

$$\|U_i\|^2 = \frac{\left(\sum_{j=1}^{p}\frac{\left[q_{ij}^{(i)\mapsto}\right]^2}{L_{ij}}(x_j - x_i)\right)^2 + \left(\sum_{j=1}^{p}\frac{\left[q_{ij}^{(i)\mapsto}\right]^2}{L_{ij}}(y_j - y_i)\right)^2 + \left(\sum_{j=1}^{p}\frac{\left[q_{ij}^{(i)\mapsto}\right]^2}{L_{ij}}(z_j - z_i)\right)^2}{\sum_{j=1}^{p}\left[q_{ij}^{(i)\mapsto}\right]^2} \tag{29}$$

Eqs. (26)-(29) above have been introduced to evaluate the macroscopic mechanical dispersion of the pore network. Mechanical dispersion as an overall outcome is contributed by the 3D convective flows occurring in channels and pores alike. In particular, provided channels with ascending flows may also form, mechanical dispersion in the pore network will also be impacted by virtue of retroflows in the vertical direction. Therefore, assessment of mechanical dispersion requires knowledge in the first place of the local scale channel ($\underline{v}_{ij}$) and pore ($\underline{v}_i$) velocity vectors and will be quantified in terms of Péclet numbers for hydrodynamic dispersion.

3.5. Method of solution

The pore network model consists of N_c equations for the total head loss (Eq. (7)) and N_p flow rate equations (Eq. (8)) being inclusive of the volumetric flux boundary condition equations $N_{p\Gamma y+}$ Eq. (18), and $N_{p\Gamma y-}$ Eq. (19). The boundary conditions also imply an additional set of $N_{p\Gamma y+}$ Eq. (16) and $N_{p\Gamma y-}$ Eq. (17) of flux-head loss equations, while with the aid of Eq. (14), the feed pressure, P_F, can be determined. The pore network introduces (i) N_p unknown pressures + feed pressure, P_F; (ii) N_c unknown network-pinned volumetric fluxes; and (iii) $N_{p\Gamma y+} + N_{p\Gamma y-}$ boundary condition fluxes. This system of non-linear equations is therefore squared. Provision of redundant Eq. (17) enables *post-facto* verification of flow rate consistency at the exit of the network in steady state. After initialization of the total head in each pore, solution of the pore network model rests on using a Newton–Raphson algorithm at two levels. In the first, knowing the poral total heads from current iteration ($\underline{\wp}^k$), channel fluxes are obtained by solving Eq. (7) (aided with Eqs. (4), Eqs. (9) and (10)). In the second, aggregation of these fluxes in the mass balance equations (Eqs. (8) and (14)) yields a vector of $N_p + 1$ residual fluxes (objective function, $\underline{\phi}(\underline{\wp}^k)$, which enables estimation of the Jacobian matrix, $J(\underline{\phi}(\underline{\wp}^k))$, of the objective function. A next iteration is resumed by estimating the new values of the pore total heads as $\underline{\wp}^{k+1} = \underline{\wp}^k - \underline{\phi}(\underline{\wp}^k).J^{-1}(\underline{\phi}(\underline{\wp}^k))$. The system is iterated until convergence is obtained on the mass conservation equations, Eqs. (8), (14), (18), and (19), with absolute residuals at most equal 10^{-11} m^3/s. Solution of the pore network model yields the static pressure in each pore of the porous medium specimen along with the volumetric fluxes in each channel. Note that Eq. (7) restores first a head loss wherefrom taking out of static pressure is straightforward. This flow field information depends on the network topology and geometry discussed above, provided all of which is known enables access to volume and ensemble averages (Eqs. (20)–(29)).

4. Results and discussion

4.1. Contraction and expansion friction loss factors

Fig. 8a and b are parity plots of calculated *versus* measured friction loss factors for sharp contraction (Fig. 8a) and sharp expansion (Fig. 8b). Eqs. (11) and (12) in Table 2 express dependence as a function of throat (or channel) Reynolds number and areal ratios of contraction/expansion. As exposed in Eqs. (11) and (12) by the different forms of the inertial/turbulent terms, contraction and expansion cannot be viewed as symmetrical phenomena. The frictional loss data were taken from Idel'chik [62] to build the required correlations. The laminar constants $C_0 = 27$, $D_0 = 26$ proposed by Idel'chik [62] were kept for the description of the viscous laminar contributions due to, respectively, the contraction and expansion in the adjacent pore bodies. Pure laminar flows in the contraction/expansion zones prevail as long as channel $Re_{ij} < 10$ (Eq. (13), Table 2). In conjunction with the necessarily laminar dissipation taking place below this limit in the channels, macroscopic rendition of laminar flows in contractions, throats and expansions is simply the well-known Darcy's law. For Re_{ij} exceeding 10^4, dissipation is governed by turbulence and the friction loss factors exhibit asymptotic dependences with respect to contraction/expansion areal ratios which are Re_{ij}-indifferent (Eqs. (11) and (12)). This is tantamount to expansion/contraction friction losses obeying quadratic flow rate dependences (Eqs. (9) and (10), Table 2). However, turbulent flows are seldom attained in usual packed bed operating conditions. Therefore, it is likely that mainly linear laminar and laminar inertial sub-regimes would manifest at the local pore-throat-pore scale. Early deviations from Darcy's law therefore will stem from (non-turbulent) quadratic terms, the manifestation of which takes place over a wide range of Re_{ij} between 10 and 10^4. In this intermediate region, there is no reason to sum up linearly the linear laminar and turbulent asymptotes in the friction loss factors. According to Churchill and Usagi [63], a general expression of the form borne by Eqs. (11) and (12) is more suitable to capture curvature over the intermediate region. Therefore, only curvature parameters n for contraction and m for expansion were fitted using Idel'chik [62] data. It was found that $n = 0.8$ and $m = 1.1$. The quality of fit can be judged from Fig. 8a and b parity plots where the envelopes represent twice the average absolute relative error

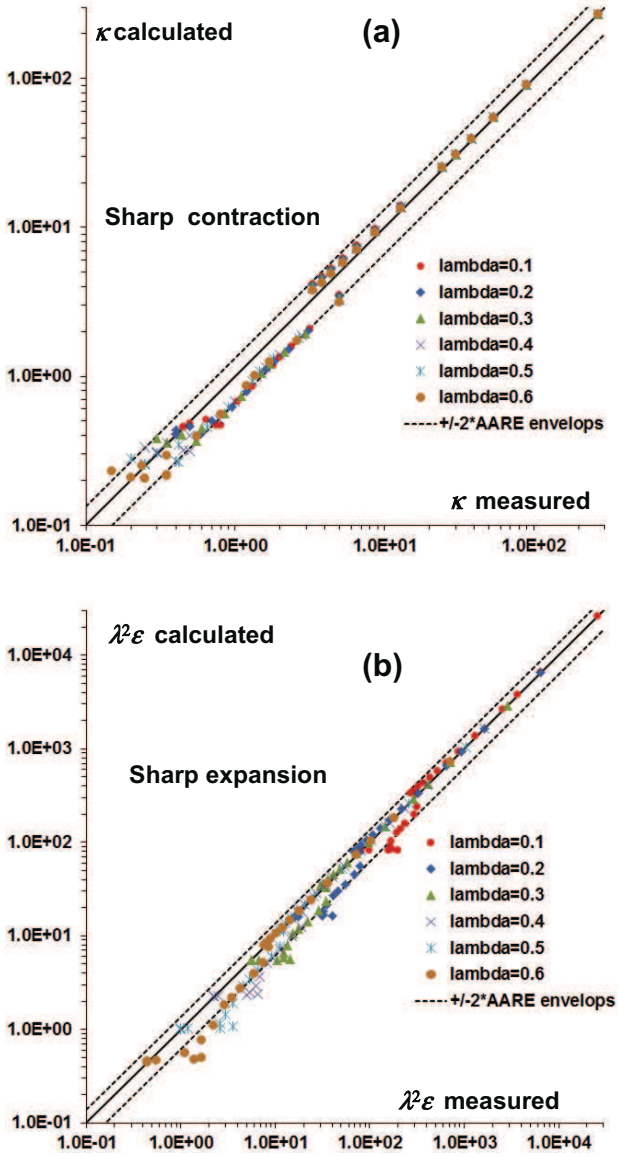

Fig. 8. Parity plots of calculated *versus* measured friction loss factors for sharp contraction (κ) & sharp expansion (ε) as a function of (channel) Reynolds number and contraction/expansion areal ratio ($\lambda = r_{cij}^2/r_i^2$), see Table 2. Data (and parameters $C_0 = 27$, $D_0 = 26$) are from Idel'chik [62], and only $n = 0.8$ & $m = 1.1$ are fitted parameters. Envelopes represent twice the average absolute relative error between measured and calculated friction factors, *i.e.*, 16.8 % for κ, 18.9 % for ε.

between measured and calculated friction factors, *i.e.*, 16.8% for κ, 18.9% for ε.

4.2. Throat effective aspect ratio

The throat circular equivalent radius introduced earlier (Fig. 3d) ignores the Venturi-like pore-throat geometry. It would predict too large a friction loss compared to that of actual biconical (converging–diverging) shapes. Hence to map the peculiar pore-throat assembly, it is useful to resort to an equivalent cylindrical channel of length l_{ij} (Fig. 3f) and effective radius r^e_{cij} such that the friction loss across the pore-throat-pore assemblage would be identical whether biconical or cylindrical throat shapes are concerned. Such correction, namely a throat effective aspect ratio, r^e_{cij}/r_{cij}, can be obtained in several manners: by means of (i) approximations of the pore-throat geometry, such as Venturi shapes [6,64]; (ii) ensemble-averaging the cross-sectional areas at each position around throat position during reconstruction as described earlier for the determination of the equivalent cylindrical length; (iii) or alternatively through one single experimental determination in the Darcy regime of the bed pressure loss for a given volumetric flow rate where the aspect ratio would correspond to the value that minimizes the error between measured and simulated pressure loss using the pore network model. The three strategies are equivalent and we illustrate the latter one in Fig. 9 where knowledge of bed pressure drop at $Re_{bed} = 10^{-2}$ enables estimation of the effective throat radius assuming that all throats are assigned the same cross-sectional shape factors. This gives a throat effective aspect ratio of 1.37 which minimizes the error between Darcy's law (laminar linear limit of Ergun equation) and pore network model predictions.

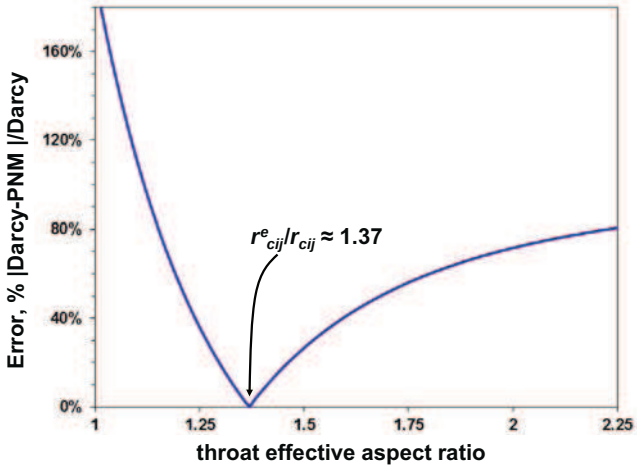

Fig. 9. Relative error between Darcy regime determination of bed pressure drop and prediction from pore network: bed packed with 4 mm spheres, $Re_{bed} = 10^{-2}$ depicting estimation of the optimal effective throat aspect ratio.

4.3. (Non-turbulent) quadratic dissipation versus acceleration/deceleration effects

Network simulations of a strongly inertial liquid flow in a bed packed with 4 mm spheres at $Re_{bed} = 10^2$ are illustrated in the form of contour plots in Fig. 10 for the poral total head field (Fig. 10a), the channel Reynolds numbers as defined by Eq. (13) (Fig. 10b), and the pore velocity head normalized with respect to local static pressure (Fig. 10c). Apart from the expected trend of the pressure field in the streamwise direction (Fig. 10a), the wide disparities displayed by the channel Reynolds numbers, Re_{ij} (Fig. 10b) are worth noting. For $Re_{bed} = 10^2$, the channel Re_{ij} varied up to 546, which, according to the ranges delineated by the contraction/expansion correlations (Eqs. (11) and (12)), suggests that in none of the network elements the flow was turbulent. However, deviation from the pure laminar case ($Re_{ij} > 10$) concerned the vast majority (78.3%) of the throat-pore-throat elements, thus unambiguously spotting the network locations subject to inertia-dominated laminar flows. In the remaining elements of the network, fluid irrigation took exclusively place in the linear laminar flow.

A fuller portrait is provided in Fig. 11 as regards the impact of Re_{bed} on the proportion of channels deviating from pure laminar flow. It is indeed the buildup of this proportion as Re_{bed} increases, which senses the manner whereby deviations from Darcy's law occur. Our model, in comprising contraction and expansion formulations associated with detailed geometry and topology information about the pore network, predicts that inasmuch as $Re_{bed} < \sim 3$, none

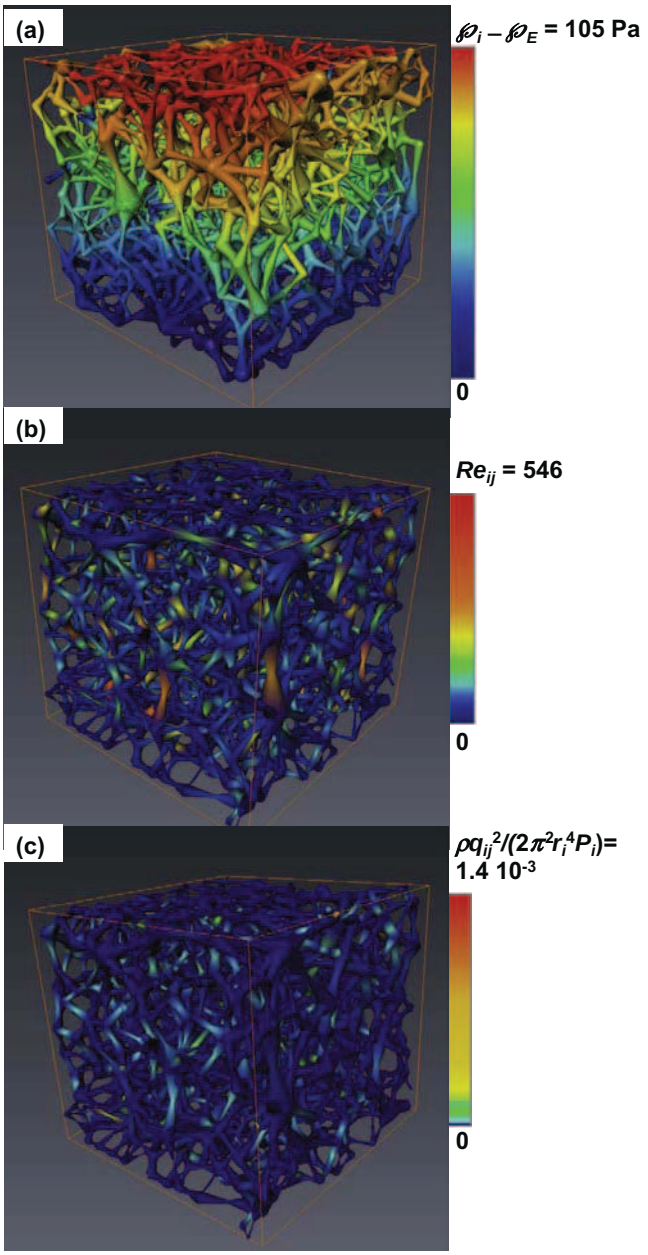

Fig. 10. (a) Total head 3D field (and direction of macroscopic flow self-evident), (b) channel Reynolds numbers (Eq. (13)), and (c) fractional pore velocity head in terms of static pressure over the porous specimen shown in Fig. 1. Simulation of strongly inertial liquid flow (ρ = 700 kg/m^3, μ = 0.001 Pa s) in a bed packed with 4 mm spheres at $Re_{bed} = 10^2$.

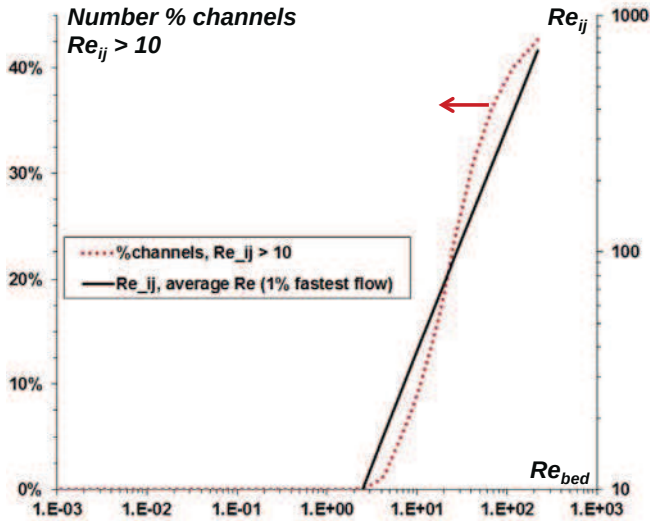

Fig. 11. Incidence of bed Reynolds number on (i) the number fraction of channels in the pore network deviating from pure laminar flow and (ii) average channel Reynolds number of the upper 1% fastest channels.

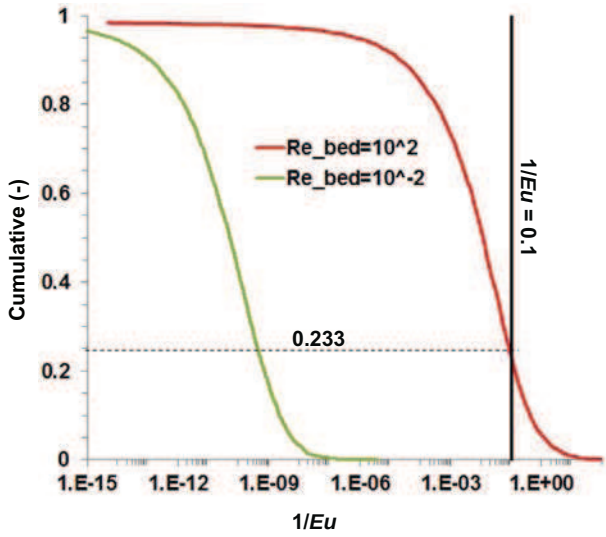

Fig. 12. Cumulative (descending) distribution of the simulated reciprocal Euler numbers for the N_c pore-throat-pore elements of the network for two bed Reynolds numbers: Darcy flow ($Re_{bed} = 10^{-2}$), strongly inertial flow ($Re_{bed} = 10^2$) over the porous specimen shown in Fig. 1.

of the network elements shall deviate from the linear Darcy's behavior (for all N_c channels, $Re_{ij} < 10$, Fig. 11). After this limit, the fraction of channels undergoing non-linear entrance/exit effects quickly climbs with Re_{bed}. Such transition from Darcy's behavior is sharp and beyond ambiguity. Anyone involved in discriminating transitions from Darcy's behavior is aware that such delineation from pressure drop – flow rate plots is quite diffuse though often bracketed between $Re_{bed} = 1$ and 10, *e.g.*, [52,54,65]. Therefore, in spite of its qualitative consistency with a large body of experimental data, this transition at $Re_{bed} \sim 3$ is unique to the network under study. It highlights how the flow meso-mechanisms are impacted by the network morphology. Changing one or some of the network topology and geometry features will reflect in an alteration of this transition. Moreover, Fig. 11 illustrates the response of the upper 1% fastest channels as a function of Re_{bed}. Their corresponding average channel Reynolds number increases nearly linearly with the bed Reynolds number but the turbulent limit is never reached across the simulated Re_{bed} range.

Deviations from linear behavior correspond to the irreversible degradation of kinetic energy as a result of fluid acceleration and deceleration nearby the element's contraction and expansion. These quadratic effects, concealed in the contraction/expansion friction losses (Eqs. (9) and (19)), are not to be confounded with the velocity head in the pore which represents to the most only a marginal fraction of the pore static pressure (Fig. 10c). A more accurate manner to evaluate how important the local accelerations/decelerations are, consists in comparing the static pressure difference, $P_i - P_j$, between all couples of adjacent pores with the change in velocity head as the fluid moves from pore i to pore j.

This difference can be evaluated in the form of an Euler number defined as:

$$Eu_{ij} = \frac{P_i - P_j}{\frac{\chi}{2\pi^2}\rho q_{ij}^2 (r_{ci}^{-4} - r_{cj}^{-4})} \tag{30}$$

Fig. 12 illustrates how important is the effect of acceleration/deceleration relative to static pressure difference for $Re_{bed} = 10^2$ and 10^{-2}. The *y*-axis represents the cumulative (descending) distribution of the simulated *reciprocal* Euler numbers, $1/Eu_{ij}$, for the N_c pore-throat-pore elements of the network. The effect of acceleration/deceleration is considered as practically negligible for $1/\mathrm{Eu} < 0.1$. This means that Eq. (6) for the total head can safely be approximated as $P_i + \rho g y_i + o(P_i)$ with an error no more than 10% on neglecting the velocity head *difference* with respect to the static pressure *difference* of any pair of interconnected pores. Expectably, acceleration/deceleration effects for $Re_{bed} = 10^{-2}$ were vanishingly small everywhere in the pore network. On the contrary, for $Re_{bed} = 10^2$, 23.3% of the pore-throat-pore elements definitely violated this approximation (Fig. 12), with some elements showing skyrocketing $1/Eu \approx 130$. Consequently, inclusion of acceleration/deceleration effects must be taken into account in pore network simulations in particular after breakup from Darcy's law regime (some $Re_{ij} > 10$) to accurately capture local static pressures at the pore scale.

4.4. Pore network macroscopic (frictional) head loss gradient versus Ergun equation

Fig. 13 displays a dissection of the dissipation contributions to the macroscopic frictional pressure drop of an air flow as predicted by means of the pore network model and expressed as a function of Re_{bed}. For illustration, simulation from the well-trodden Ergun equation is also shown for a set of laminar constant = 150 and quadratic constant = 1.75. This set is known to work well for unconsolidated packs of isometric (spherical) grains. Silencing in Eq. (6) the contraction and expansion friction loss term, C_{ij} and E_{ij}, highlights the linear laminar behavior arising solely from the channel viscous flow (Fig. 13). The previous analysis instructed the fact that channel-based Reynolds numbers are unlikely to exceed the pipe-flow limit of 2400 for typical packed bed operation. Channel flow contribution therefore is not expected to alter the linear laminar trend of the macroscopic head loss gradient. Moreover, a minor contribution of channel dissipation is scored over the simulated range of bed Reynolds numbers as displayed in Fig. 13. Alternatively, simulating the pore network by keeping either the contraction mechanism or the expansion mechanism, while disabling the channel viscous mechanism, gives rise to linear dissipation behavior in the Re_{bed} lower range. This indicates that linear laminar flow resistances are also contributed by the adjacent pores *via* constrictions and expansions as described in Eqs. (11) and (12). Moreover, lack of similarity of the inertial/turbulent terms as exposed in Eqs. (11) and (12) translates, for the Re_{bed} upper range, into different dissipation levels of expansions *versus* contractions (Fig. 13). Also, inclusion in Eq. (7) of contraction and expansion features appears to be an adequate assumption to bring about deviations from the linear laminar behavior of the frictional pressure drop response. It is worth noting that contraction or expansion dissipations outweigh significantly channel dissipation especially at high Re_{bed}. Thus it is crucial to include in pore network modeling non-linear features associated with upstream and downstream areal changes in the pore-throat-pore elements when Re_{bed} lies outside the validity range of Darcy's law. Finally, pore network simulations including the whole set of mechanisms in Eq. (7) predict remarkably accurately the macroscopic frictional pressure drop as given by Ergun-like equation (Fig. 12) over a wide range of Re_{bed}.

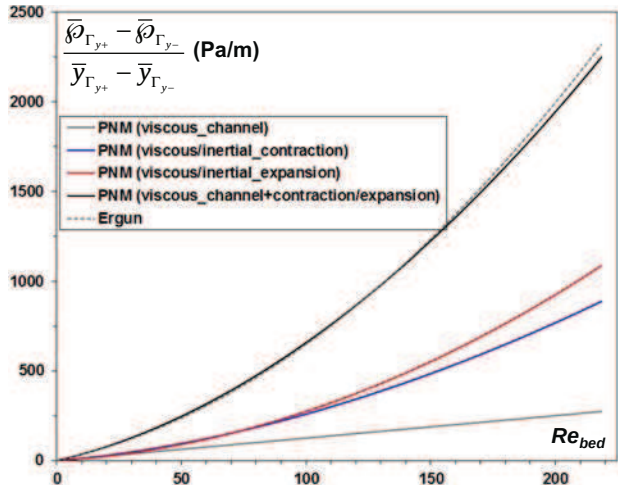

Fig. 13. Pore network predictions of macroscopic head loss gradient for air flow ($\rho = 1.2$ kg/m^3, $\mu = 1.78\ 10^{-5}$ Pa s), assessment of the relative importance of Darcy and non-Darcy (expansion/contraction) terms, and comparison with Ergun-like correlation macroscopic pressure gradient correlation.

4.5. Pore network mechanical dispersion

The degree of heterogeneity of the pore network can be made sense of from the coefficients of variation for the throat and pore radii, and throat lengths given in Table 1. These *COV* values, comprised between 0.4 and 0.5, reflect quite an important heterogeneity in comparison to homogeneous networks (*COV* = 0). Such structural heterogeneity of the network is known to cause dispersion. Moreover, it is of importance to realize that only the *mesoscopic* level of this heterogeneity is echoed in the network energy and mass balances Eqs. (7) and (8) above. That is, the microscopic scale of advection *inside* the pores and channels cannot be resolved in this formulation, either because it is lost in the integrations or because of the flow approximations resorted to for describing the contraction/expansion terms or the inner-pore hydrodynamics. In terms familiar to chemical engineers, the pore network model views channel flows as a 3D array of local plug flows while it is clueless about the fluid dynamics and mixedness state in the pores themselves. Encompassing the full spectrum of dispersion is beyond this study's scope as it would have required inclusion of molecular diffusion and solving at the *microscopic* level the passive scalar advection–diffusion transport inside each individual pore-throat-pore element to catch on the-so-called Aris-Taylor dispersion [9]. This was not the purpose of current work for which single-phase flows in a complex 3D geometry such as ours would have demanded far more elaborate computational and (fluid–fluid and fluid-network) interaction rules.

By construction, our steady-state pore network model captures only part of the macroscopic mechanical dispersion; the one inherited, *via* network ensemble averaging, from the mesoscopic flow discrepancies at the pore-throat-pore level. Neglect of microscopic advection–diffusion coupling is anticipated to yield macroscopic dispersion that is lower than actual one. Similarly, too simplified a picture of pore-scale flow and fluid convective mixedness, as reflected by the simplified assumptions subtending Eqs. (29) and (30), might not be sufficient and would in all likelihood lead to an underestimation of mechanical dispersion. The importance of such bias will be assessed by computing pore network longitudinal and transverse Péclet numbers and comparing them to state-of-art knowledge in the area of dispersion in porous media. Also, the role of non-linear laminar phenomena in prompting dispersive effects

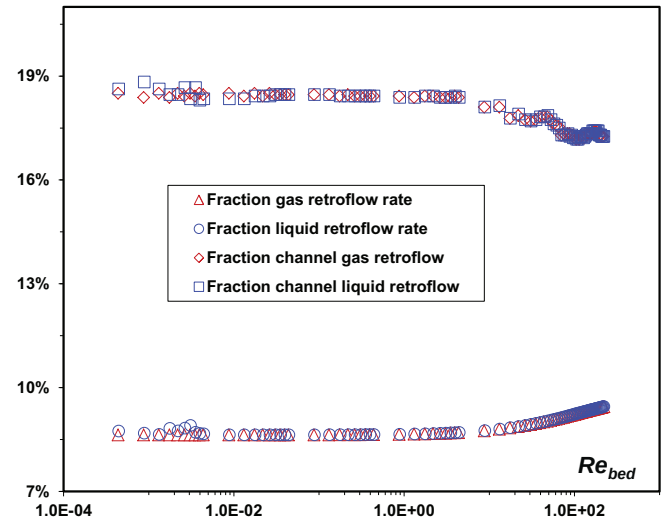

Fig. 14. Pore network predictions of the number and flow-rate fractions of retroflow channels for gas ($\rho = 1.2$ kg/m^3, $\mu = 1.78\ \ 10^{-5}$ Pa s) and liquid ($\rho = 700$ kg/m^3, $\mu = 10^{-3}$ Pa s) flows in Darcy and non-Darcy flow regimes.

potentially deviating from those known to prevail in Darcy's regime will be discussed below.

Fig. 14 portrays the dependence between the bed Reynolds number and the number fraction of channels manifesting gas and liquid retroflows (channel ascending flow). The percentage of retroflow channels was invariant in Darcy flow corresponding to *ca.* 19% for our particular network. Beyond $Re_{bed} \sim 3$ transition, quadratic effects brought about weak Re_{bed} dependence with negative correlation; though the decline in retroflow proportion was limited up to $Re_{bed} \sim 250$. This waning is coherent with dominance of macroscopic descending flow imposed on the network. However, the lesser fraction of ascending channels in non-Darcy flow mirrors a larger statistical fraction of fluid flow rate events as shown in Fig. 13 whether gas or liquid is concerned. The retroflow rate fraction is invariant in Darcy flow, around 8%, but showcases an increase upon inception of inertial (non-Darcy) effects after $Re_{bed} \sim 3$. Occurrence of retroflows in our pore network simulations exemplifies in intuitive terms manifestation of mechanical dispersion at the macroscopic level nuancing the latter in Darcy and non-Darcy flows.

Let us examine the evolution as a function of Re_{bed} of the 3D ensemble-average velocity and root-mean square velocity components in the throats (Eqs. (26) and (27)) and pores (Eqs. (29) and (30)) of the network (Fig. 15a–c). Pore network simulations predict expectably pore vertical average velocity, $\langle v_{py} \rangle$, lower than its channel counterpart, $\langle v_{cy} \rangle$. Also, the average channel velocity components in the directions normal to main flow are close to zero as should be expected. This is unlike the x and z pore average velocity components, especially $\langle v_{px} \rangle$. This signifies that the combination rules implemented by Eqs. (29)-(29) are not fully adequate, and that capture of realistic poral fluid velocity field would require more accurate pore fluid dynamic hypotheses. Another feature of the pore network simulations is the prediction of quasi-isotropic spatially fluctuating velocity components, in streamwise and transverse directions, for channels and pores alike. It is logical to expect that the state of mixedness to prevail within pores would approach that of a CSTR and even more so in non-Darcy flows. Even though Fig. 15d highlights an increase of the pore root-mean-square velocity components as a function of Re_{bed}, it was not sufficient to induce stronger dispersion as compared to that contributed by the ensemble of channels.

The ratios $\langle v_{cy} \rangle / \langle v'_{c\alpha} \rangle$ and $\langle v_{py} \rangle / \langle v'_{p\alpha} \rangle$ merely represent for each direction the Péclet number that quantifies the extent of directional mechanical dispersion. The common normalizing velocity (*i.e.*, $\langle v_{cy} \rangle$ or $\langle v_{py} \rangle$) of the directional root-mean-square velocities yields transverse and longitudinal Péclet numbers that are indifferent to spatial directions likening the pattern noted for the root-mean-square velocities above (Fig. 15c and d). However, an isotropic mechanical dispersion as predicted by the pore network mode is at odds with the well-known fact that longitudinal dispersion outperforms transverse dispersion, typically by a factor 5 in advection dominated flows [66].

Fig. 16 exemplifies the dependence between Re_{bed} and longitudinal dispersions (Pe_L) for channel ($=\langle v_{cy} \rangle / \langle v'_{c\alpha} \rangle$), poral ($=\langle v_{py} \rangle / \langle v'_{p\alpha} \rangle$) and channel-pore aggregated contributions, to reflect their relative weights in the macroscopic dispersion resulting from the set of pore-channel-pore mesoscopic elements. Up to $Re_{bed} \sim 3$, the exponent of the scaling law relating Re_{bed} to Pe_L as predicted from the pore network model is zero meaning that mechanical dispersion is proportional to the streamwise average (or interstitial) velocity.

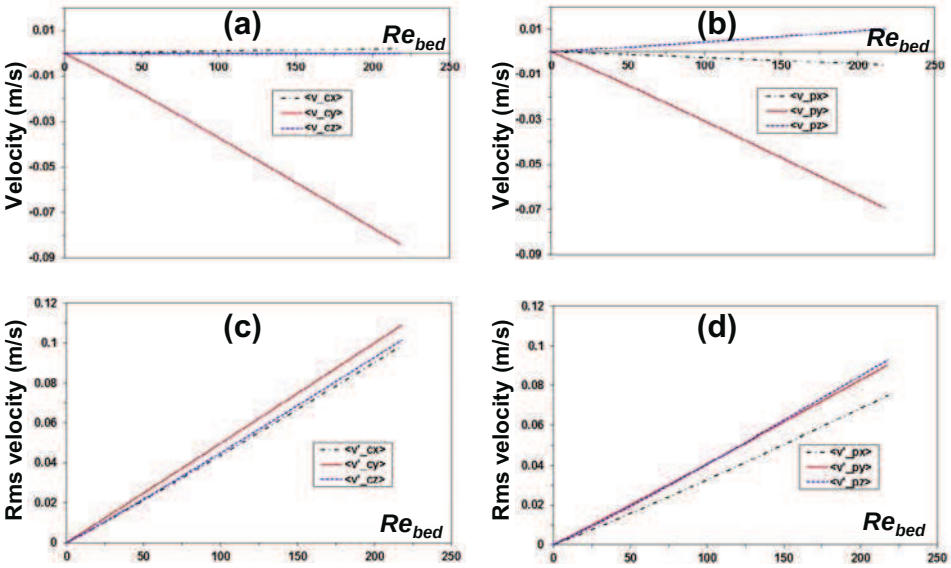

Fig. 15. Pore network simulations of the ensemble-average channel (a) and pore (b) 3D ($\alpha = x, y, z$) velocity components ($\langle v_{c\alpha} \rangle$, $\langle v_{p\alpha} \rangle$) and their corresponding root-mean square velocity ($\langle v'_{c\alpha} \rangle$ (c), $\langle v'_{p\alpha} \rangle$ (d)) components as a function of bed Reynolds number.

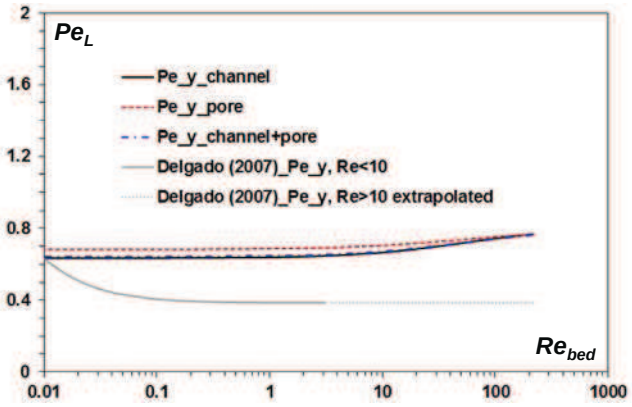

Fig. 16. Pore network prediction of the behavior of longitudinal mechanical dispersion contributed by channels, pores and their combination in Darcy and non-Darcy flow regimes, and comparison with Delgado's [66] correlation for longitudinal Péclet number in porous media.

Bruderer and Bernabé [9] observed such linear behavior over a wide range of Reynolds numbers for longitudinal dispersion in 2D arrays of square capillaries exhibiting important structural heterogeneity comparable to ours, *i.e.*, $COV > 0.5$ (Table 1). In 3D porous media, according to the comprehensive compilation of Pe_L by Delgado [66,67], such scaling law is fulfilled piecewise: (i) in the so-called predominant mechanical dispersion regime valid mainly over Darcy's law upper range, in our case up to $Re_{bed} < 3$, and (ii) in the pure mechanical dispersion regime, $Re_{bed} > 3$ assigned to inertia-dominated flows, where Pe_L levels off at a value of 2 at high bed Reynolds numbers.

For the purpose of comparison, we plotted in Fig. 16 a general correlation by Delgado [66] for longitudinal dispersion in packed beds corresponding to a regime with dominant mechanical dispersion ($Re_{bed} < 3$). The pore network model captures quite well the behavior of the longitudinal dispersion (Pe_L) in laminar and moderately inertial flows. Delgado's correlation predicted Pe_L range between 0.4 and 1, whereas the pore network Pe_L plateaus at 0.6 for $Re_{bed} < 3$. We could not compare pore network Pe_L to Delgado's correlation under purely mechanical controlled flows ($Re_{bed} > 3$) as his correlation possibly contained typesetting errors in the published form (their Eq. (16), P.1250). Therefore, we merely extrapolated the correlation for dominant mechanical dispersion towards higher Re_{bed} (dotted line in Fig. 16). For $Re_{bed} > 3$, the pore network model predicted an increase in mechanical dispersion in qualitative accordance with tracer experiments of dispersion in porous media at high bed Reynolds numbers [67]. However, such increase was insufficient to reach $Pe_L = 2$ which characterizes inertia dominated flows. These findings confirm that extension of pore network modeling to simulate the full range of macroscopic mechanical dispersion in heterogeneous networks is doomed to failure if an appropriate description at a mesoscopic level of pore fluid dynamics is not provided.

5. Conclusion

The local properties of an isometric bead pack were determined experimentally by means of a high-resolution X-ray micro-tomography imaging technique. A three-dimensional irregular and unstructured pore network was then extracted and thoroughly characterized in terms of topology and geometry by establishing the needed distributions for pore bodies, throats, channels and connectivity. A particular emphasis was put on modeling, simulating and analyzing the non-turbulent non-Darcy flows. The outlined methodology of getting the structure through micro-tomography and then using a theoretical approach for flow description is general to be applied to samples with different microstructures.

For the description of non-Darcy flows in the obtained pore network, mechanical energy balances were formulated at the level of pore-throat-pore mesoscopic elements. The non-linear inertial flow signatures were captured on the basis of flow analogies with friction loss through sudden contractions and expansions. Constitutive equations derived for contraction and expansion losses were elaborated and validated using experimental data.

The pore-level pressure and velocity information yielded from solving the network model enabled construction of macroscopic analogs by volume and ensemble averaging over the entire network domain. The model enabled access to a variety of properties such as the contribution of non-turbulent quadratic dissipation and acceleration/deceleration across the channels, the contributions to the macroscopic frictional loss of the different mechanisms at the channel and pore scales, and the various components of channel and pore mechanical dispersion.

The following consolidated conclusions emerge from the study:

- The wealth of detailed topology and geometry information obtained from X-ray imaging and implemented in the pore network model successfully captured the moment and extent of takeover by laminar non-linear phenomena. From isolating the channel events with channel Reynolds numbers in excess of 10, inception of non-Darcy flows was detected to occur at a bed Reynolds number equal 3 for our particular bead pack.
- The average channel Reynolds number of the 1% fraction of the fastest channel flow events increased linearly with bed Reynolds number (or cumulative flow rate) but with no sign that turbulence occurred either in contractions, expansions or throats ($Re_{ij} \ll 10^4$).
- The pattern of local Euler numbers revealed that the contribution of pore–pore velocity head difference to total head difference becomes important for $Re_{bed} > 3$. The consequence is a necessity to account for the acceleration/deceleration term in the mechanical energy balances to properly estimate the static pressure field in the network.
- The pore network model provided remarkably good predictions of the trend of macroscopic frictional loss gradient in terms of contributions by the pore and channel linear losses, and the contraction and expansion quadratic losses. It was observed that the linear losses attributed only to channel flow was a marginal portion of the overall frictional loss for non-Darcy flows.
- As a part and parcel of macroscopic mechanical dispersion, the level of details of the network model was sufficient to resolve all the channels exhibiting a retroflow behavior opposite to the dominant macroscopic flow direction. However, the model predicted quasi-isotropic mechanical dispersions in channels and pores alike. For channels, experimental evidence contradicts such findings as transverse Péclet numbers are typically *ca.* 5 times lower than their longitudinal counterparts. According to the network model, poral dispersion was not sufficient to induce stronger dispersion as compared to that contributed by the ensemble of channels. This led to an overall mechanical dispersion that was lower than that predicted from literature tracer-based Pe_L correlations. In future works, extension of pore network modeling to simulate the full range of macroscopic mechanical dispersion in heterogeneous networks will require finer descriptions at the mesoscopic level of pore fluid dynamics. Validations could also be performed for the numerical residence time distributions (RTDs) simulated from the pore network which can be compared to experimentally determined RTDs.

Acknowledgments

Two of the authors wish to thank IFPEN for the visiting scientist (FL) and postdoctoral (RH) fellowships. M. Rolland (IFPEN, Solaize) is greatly acknowledged for fruitful discussions on pore network modeling.

References

[1] M.J. Blunt, M.D. Jackson, M. Piri, P.H. Valvatne, Detailed physics, predictive capabilities and macroscopic consequences for pore-network models of multiphase flows, Adv. Water Resources 25 (2002) 1069–1089.
[2] I. Fatt, The network model of porous media I. Capillary pressure characteristics, Pet. Trans. AIME 207 (1956) 144–159.
[3] S. Bryant, M. Blunt, Prediction of relative permeability in simple porous media, Phys. Rev. A 46 (1992) 2004–2011.
[4] M.A. Ioannidis, I. Chatzis, Network modeling of pore structure and transport properties of porous media, Chem. Eng. Sci. 48 (1993) 951–972.
[5] T.W. Patzek, Verification of a complete pore network simulator of drainage and imbibition, SPE J. 6 (2001) 144–156.
[6] K.E. Thompson, H.S. Fogler, Modeling flow in disordered packed beds from pore-scale fluid mechanics, AIChE J. 43 (1997) 1377–1389.
[7] C. Jia, K. Shing, Y.C. Yortsos, Advective mass transfer from stationary sources in porous media, Water Resour. Res. 35 (1999) 3239–3251.
[8] A. Ahmadi, A. Aigueperse, M. Quintard, Calculation of the effective properties describing active dispersion in porous media: from simple to complex unit cells, Adv. Water Resour. 24 (2001) 423–438.
[9] C. Bruderer, Y. Bernabé, Network modeling of dispersion: Transition from Taylor dispersion in homogeneous networks to mechanical dispersion in very heterogeneous ones, Water Resour. Res. 37 (2001) 897–908.
[10] V. Joekar-Niasar, M. Prodanovic, D. Wildenschild, S.M. Hassanizadeh, Network model investigation of interfacial area, capillary pressure and saturation relationships in granular porous media, Water Resour. Res. 46 (W06526) (2010) 1–18.
[11] V. Joekar-Niasar, S.M. Hassanizadeh, Effect of fluids properties on non-equilibrium capillarity effects: Dynamic pore-network modeling, Int. J. Multiphas. Flow 37 (2011) 198–214.
[12] D. Bauer, S. Youssef, M. Han, S. Bekri, E. Rosenberg, M. Fleury, O. Vizika, From computed microtomography images to resistivity index calculations of heterogeneous carbonates using a dual-porosity pore-network approach: Influence of percolation on the electrical transport properties, Phys. Rev. E 84 (011133) (2011) 1–12.
[13] S. Whitaker, Theory and Applications of Transport in Porous Media, Kluwer Academic Press, Dordrecht, The Netherlands, 1999.
[14] M.J.S. de Lemos, Turbulence in Porous Media – Modeling and Applications, Elsevier, Amsterdam, The Netherlands, 2006.
[15] G.F. Pinder, W.G. Gray, Essentials of multiphase flow and transport in porous media, John Wiley & Sons Inc, New Jersey, USA, 2008.
[16] C. Boyer, A. Koudil, P. Chen, M.P. Dudukovic, Study of liquid spreading from a point source in a trickle bed via gamma-ray tomography and CFD simulation, Chem. Eng. Sci. 60 (2005) 6279–6288.
[17] Y. Sholokhova, D. Kim, W.B. Lindquist, Network flow modeling via lattice-Boltzmann based channel conductance, Adv. Water Res. 32 (2009) 205–212.
[18] A.M. Tartakovsky, P. Meakin, A smoothed particle hydrodynamics model for miscible flow in three-dimensional fractures and the two-dimensional Rayleigh–Taylor instability, J. Comput. Phys. 207 (2005) 610–624.
[19] M. Prodanovic, S.L. Bryant, A level set method for determining critical curvatures for drainage and imbibition, J. Colloid Interface Sci. 304 (2006) 442–458.
[20] C.W. Hirt, B.D. Nichols, Volume of fluid (VOF) method for the dynamics of free boundaries, J. Comput. Phys. 39 (1981) 201–225.
[21] P. Horgue, F. Augier, P. Duru, M. Prat, M. Quintard, Experimental and numerical study of two-phase flows in arrays of cylinders, Chem. Eng. Sci. 102 (2013). 335-34.
[22] F. Augier, A. Koudil, A. Royon-Lebeaud, L. Muszynski, Q. Yanouri, Numerical approach to predict wetting and catalyst efficiencies inside trickle bed reactors, Chem. Eng. Sci. 65 (2010) 255–260.
[23] M.P. Dudukovic, F. Larachi, P.L. Mills, Multiphase catalytic reactors: a perspective on current knowledge and future trends, Catal. Rev. Sci. Eng. 44 (2002) 123–246.
[24] F. Augier, C. Laroche, E. Brehon, Application of computational fluid dynamics to fixed bed adsorption calculations: Effect of hydrodynamics at laboratory and industrial scale, Sep. Purif. Technol. 63 (2008) 466–474.
[25] P.S. Gomes, M. Minceva, A.E. Rodrigues, Simulated moving bed technology: old and new, Adsorption 12 (2006) 375–392.
[26] F. Augier, F. Idoux, J.Y. Delenne, Numerical simulations of transfer and transport properties inside packed beds of spherical particles, Chem. Eng. Sci. 65 (2010). 1055-10.
[27] Z. Zeng, R. Grigg, Criterion for non-Darcy flow in porous media, Transp. Porous Media 63 (2006) 57–69.
[28] Y.-S. Wu, B. Lai, J.L. Miskimins, P. Fakcharoenphol, Y. Di, Analysis of multiphase non-Darcy flow in porous media, Transp. Porous Media 88 (2011) 205–223.
[29] J. Zhang, H. Xing, Numerical modeling of non-Darcy flow in near-well region of a geothermal reservoir, Geothermics 42 (2012) 78–86.
[30] G. Radilla, A. Nowamooz, M. Fourar, Modeling non-Darcian single- and two-phase flow in transparent replicas of rough-walled rock fractures, Transp. Porous Media 98 (2013) 401–426.
[31] M. Fourar, R. Lenormand, F. Larachi, Extending the F-function concept to two-phase flow in trickle beds, Chem. Eng. Sci. 56 (2001) 5987–5994.
[32] G. Radilla, M. Fourar, F. Larachi, Correlating gas-liquid co-current flow hydrodynamics in packed beds using the F-function concept, J. Chem. Technol. Biotechnol. 80 (2005) 107–112.
[33] E.F. Blick, F. Civan, Porous media momentum equation for highly accelerated flow, SPE Reserv. Eng. 3 (1988) 1048–1052.
[34] O. Molerus, A coherent representation of pressure drop in fixed beds and of bed expansion for particulate fluidized beds, Chem. Eng. Sci. 35 (1980) 1331–1340.
[35] J.P. Du Plessis, J.H. Masliyah, Mathematical modeling of flow through consolidated isotropic porous media, Transp. Porous Media 3 (1988) 145–161.
[36] O. Molerus, J. Schweintzer, Resistance of particle beds at Reynolds numbers up to Re$\sim 10^4$, Chem. Eng. Sci. 44 (1988) 1071–1079.
[37] H. Ma, D.W. Ruth, The microscopic analysis of high Forchheimer number flow in porous media, Transp. Porous Media 13 (1993) 139–160.
[38] J.A. Andrade Jr, U.M.S. Costa, M.P. Almeida, H.A. Makse, H.E. Stanley, Inertial effects on fluid flow through disordered porous media, Phys. Rev. Lett. 82 (1998) 5249–5252.
[39] E. Sanchez-Palencia, On the asymptotics of the fluid flow past an array of fixed obstacles, Int. J. Eng. Sci. 20 (1982) 1291–1301.
[40] S. Whitaker, Flow in porous media I: a theoretical derivation of Darcy's law, Transp. Porous Media 1 (1986) 3–35.
[41] J.-C. Wodié, T. Lévy, Correction non linéaire de la loi de Darcy, C. R. Acad. Sci. Paris 312 (II) (1991) 157–161.
[42] C.C. Mei, J.L. Auriault, The effect of weak inertia on flow through a porous medium, J. Fluid Mech. 222 (1991) 647–663.
[43] D. Lasseux, A.A.A. Arani, A. Ahmadi, On the stationary macroscopic inertial effects for one phase flow in ordered and disordered porous media, Phys. Fluids 23 (2011) 073103. http://dx.doi.org/10.1063/1.3615514.
[44] S. Whitaker, The Forchheimer equation: A theoretical development, Transp. Porous Media 25 (1996) 27–61.
[45] K. Yazdchi, S. Luding, Towards unified drag laws for inertial flow through fibrous mate, Chem. Eng. J. 207–208 (2012) 35–48.
[46] T. Masuoka, Y. Takatsu, Turbulence model for flow through porous media, Int. J. Heat Mass Tran. 39 (1996) 2803–2809.
[47] M. Pedras, M.J.S. de Lemos, Macroscopic turbulence modeling for incompressible flow through undeformable porous media, Int. J. Heat Mass Tran. 44 (2001) 1081–1093.
[48] F. Thauvin, K.K. Mohanty, Network modeling of non-Darcy flow through porous media, Transp. Porous Media 31 (1998) 19–37.
[49] V. Joekar-Niasar, S.M. Hassanizadeh, Analysis of fundamentals of two-phase flow in porous media using dynamic pore-network models: a review, Crit. Rev. Environ. Sci. Technol. 42 (2012) 1895–1976.
[50] X. Wang, F. Thauvin, K.K. Mohanty, Non-Darcy flow through anisotropic porous media, Chem. Eng. Sci. 54 (1999) 1859–1869.
[51] H.W. Lao, H.J. Neeman, D.V. Papavassiliou, A pore network model for the calculation of non-Darcy flow coefficients in fluid flow through porous media, Chem. Eng. Commun. 191 (2004) 1285–1322.
[52] R.B. Bird, W.E. Stewart, E.N. Lightfoot, Transport Phenomena, second ed., John Wiley & Sons Inc., New Jersey, USA, 2002.
[53] A.A. Martins, P.E. Laranjeira, J.C.B. Lopes, M.M. Dias, Network modeling of flow in a packed bed, AIChE J. 53 (2007) 91–107.
[54] G. Schneebeli, Expériences sur la limite de validité de la loi de Darcy et l'apparition de la turbulence dans un écoulement de filtration, La Houille Blanche 2 (1955) 141–149.
[55] M.A. Latifi, N. Midoux, A. Storck, J.N. Gence, The use of micro-electrodes in the study of flow regimes in a packed-bed reactor with single-phase liquid flow, Chem. Eng. Sci. 44 (1989) 2501–2508.
[56] M.T. Balhoff, M.F. Wheeler, A predictive pore-scale model for non-Darcy flow in porous media, SPE J. 14 (2009) 579–587.
[57] S. Youssef, E. Rosenberg, N. Gland, S. Bekri, O. Vizika, Quantitative 3D characterisation of the pore space of real rocks: Improved μ-CT resolution and pore extraction methodology, Int. Sym. Soc. Core Analysts, Calgary, Sept 10–12 (2007) paper SCA2007-17.
[58] S. Youssef, M. Han, D. Bauer, E. Rosenberg, S. Bekri, M. Fleury, O. Vizika. High resolution μ-CT combined to numerical models to assess electrical properties of bimodal carbonates, Int. Sym. Soc. Core Analysts, Abu-Dhabi, UAE, 29 October–2 November, 2008, paper SCA2008-37.
[59] C. Fouard, F. Cassot, G. Malandain, C. Mazel, S. Prohaska, D. Asselot, M. Westerhoff, J.P. Marc-Vergnes, Skeletonization by blocks for large 3D datasets: Application to brain microcirculation, Biomedical Imaging: Nano to Macro, IEEE Int. Symp. 1 (2004) 89–92.
[60] F. Cassot, F. Lauwers, C. Fouard, S. Prohaska, V. Lauwers-Cances, A novel three-dimensional computer-assisted method for a quantitative study of microvascular networks of the human cerebral cortex, Microcirculation 13 (2006) 15–32.
[61] D. Bauer, S. Youssef, M. Fleury, S. Bekri, E. Rosenberg, O. Vizika, Improving the estimations of petrophysical transport behavior of carbonate rocks using a dual pore network approach combined with computed microtomography, Transp. Porous Med. 94 (2012) 505–524.

[62] I.E. Idel'chik, Memento des pertes de charge – Coefficients de pertes de charge singulières et de pertes de charge par frottement, Eds. Eyrolles, Paris, France, 1999.
[63] S.W. Churchill, R. Usagi, A general expression for the correlation of rates of transfer and other phenomena, AIChE J. 18 (1972) 1121–1128.
[64] T.R. Melli, L.E. Scriven, Theory of two-phase cocurrent downflow in networks of passages, Ind. Eng. Chem. Res. 30 (1991) 951–969.
[65] M.K. Hubbert, Darcy law and the field equations of the flow of underground fluids, Trans. Am. Inst. Min. Mandal. Eng. 207 (1956) 222–239.
[66] J.M.P.Q. Delgado, Longitudinal and transverse dispersion in porous media, Chem. Eng. Res. Des. 85 (2007) 1245–1252.
[67] J.M.P.Q. Delgado, A critical review of dispersion in packed beds, Heat Mass Transfer 42 (2006) 279–310.